



ATLAS NOTE

ATLAS-CONF-2013-064

July 13, 2013



Identification of Hadronic Decays of Tau Leptons in 2012 Data with the ATLAS Detector

The ATLAS Collaboration

Abstract

The study of final states containing hadronically decaying tau leptons is an important and growing part of the ATLAS physics program. At the center of this are the ATLAS tau reconstruction and identification algorithms, which are used to identify hadronically decaying tau leptons and reject various backgrounds. The basic principles behind these algorithms are described in this document. Estimates of the signal efficiency and background rejection based on studies of simulations and data samples are provided. For a sample identification efficiency of 35%, rejection factors against multi-jet backgrounds of the order of 60 to 500 are achieved. Data-driven methods are used to provide scale factors which can be used to adjust the signal efficiency in simulation samples. Good agreement is found between the tau identification efficiency in data and simulations. The corresponding scale factors are measured with a precision of the order of 2-3% in the most sensitive channel.

1 Introduction

Tau leptons are the heaviest known leptons, with a mass of 1.777 GeV [1]. With a proper decay length of $87\text{ }\mu\text{m}$, they decay before reaching the detector and can only be identified through the reconstruction of their decay products. Due to their high mass, tau leptons are the only leptons for which decay modes involving hadrons are allowed. This unique property leads to the division of the different tau decay modes into two categories, *leptonic* and *hadronic*. The leptonic mode τ_{lep} , where the tau decays into two neutrinos and either an electron ($\tau \rightarrow e\nu_e\nu_\tau$) or a muon ($\tau \rightarrow \mu\nu_\mu\nu_\tau$), represents 35% of all tau decays. In this mode, the decay products cannot be distinguished from prompt electrons or muons. For this reason, the leptonic decay mode is not considered for tau identification. The hadronic mode τ_{had} represents the remaining 65% of all tau decays. In this mode, the tau decays into a tau neutrino, accompanied predominantly by charged and neutral pions, and rarely by kaons. The neutrino remains undetected, leaving only the hadrons to be used for reconstruction and identification¹. The hadrons are reconstructed as a jet of particles in the detector, which makes it very hard to distinguish hadronic tau decays from gluon- or quark-initiated *jets*. The narrow shower shape and the distinct number of tracks characteristic of hadronic tau decays are useful in discriminating such decays from other signatures in the detector. The hadronic decay is classified into *1-prong* decays with one track, and *3-prong* decays with three tracks. The number of produced neutral pions is currently not considered for tau identification.

Hadronically decaying tau leptons play an important role in physics analyses in ATLAS. Their field of application reaches from Standard Model measurements [2, 3, 4, 5], including Higgs searches [6, 7, 8], to searches for physics beyond the Standard Model [9, 10, 11]. Therefore, the $\tau_{\text{had-vis}}$ reconstruction and identification algorithms have to be continuously improved and adjusted for the most up-to-date running conditions. For the 2012 data-taking period, the $\tau_{\text{had-vis}}$ reconstruction and identification schemes have been specifically re-optimized for the high number of simultaneous collisions per proton-proton bunch crossing (pile-up).

Two independent methods for the discrimination of $\tau_{\text{had-vis}}$ against jets are discussed: a projective likelihood method (LLH) and boosted decision trees (BDT). A BDT is also used for the rejection of electrons mis-identified as $\tau_{\text{had-vis}}$. A cut-based approach is used for the rejection of muons.

The identification efficiency of $\tau_{\text{had-vis}}$ is studied in data using a tag-and-probe approach. From these studies, a set of scale factors is derived to correct the simulated data samples used in ATLAS analyses. These measurements are performed independently using $Z \rightarrow \tau\tau$, $W \rightarrow \tau\nu$ and $t\bar{t} \rightarrow \tau + \text{jets}$ events. Scale factors for the $\tau_{\text{had-vis}}$ mis-identification probability for electrons are also measured, comparing $Z \rightarrow ee$ events in data and simulations.

The background efficiency of the identification algorithms is very sensitive to various factors (kinematics, final-state topology, flavor of the initiating parton, etc.). It must therefore be measured in a dedicated way for each specific analysis. Scale factors for background samples are therefore not presented in this note.

The data studies presented in this document are performed using data collected with the ATLAS detector [12] during the 8 TeV proton-proton collisions at the LHC [13] in 2012. Only data taken with good detector conditions are considered. Simulated Z , W , and $t\bar{t}$ events are produced using the generators PYTHIA [14] and ALPGEN [15]. PYTHIA is also used to produce Z' samples with masses of 250 GeV, 500 GeV, 750 GeV, 1000 GeV and 1250 GeV. The response of the ATLAS detector is simulated using GEANT4 [16] with the QGSP_BERT shower model [17, 18, 19] for the description of the hadronic shower. Additionally, samples simulated using the QGSP and FTFP_BERT shower model [20] are used for the estimation of systematic uncertainties.

¹The visible part of a hadronic tau decay will be referred to as $\tau_{\text{had-vis}}$ in the remainder of this note.

2 Reconstruction of Hadronic Tau Decays

The detector signature of hadronically decaying tau leptons is similar to the signature associated with jets and other leptons. It is therefore important to use combined information from many sub-detectors to reconstruct hadronically decaying taus and differentiate them from objects with similar detector signatures. In order to fulfill this requirement, a dedicated reconstruction algorithm is used for $\tau_{\text{had-vis}}$, combining both tracking and calorimeter information. This section describes the basic reconstruction of hadronic tau decays in ATLAS.

2.1 Overview of $\tau_{\text{had-vis}}$ Reconstruction

The $\tau_{\text{had-vis}}$ reconstruction in ATLAS is seeded from reconstructed jet-objects by considering each jet-object as a $\tau_{\text{had-vis}}$ candidate. The list of calorimeter clusters associated to each $\tau_{\text{had-vis}}$ candidate is then refined and used to calculate kinematic quantities. Tracks satisfying dedicated selection criteria are associated to the calorimeter clusters. Identification variables are then calculated using both tracking and calorimeter information. These variables are combined into multi-variate discriminants to reject fake $\tau_{\text{had-vis}}$ candidates from jets and leptons. Finally, pre-defined selection criteria, based on the output of the discriminants, are used at the analysis level to select a sample of $\tau_{\text{had-vis}}$ candidates with the desired level of background rejection and signal efficiency.

2.2 Reconstruction Seeds

The $\tau_{\text{had-vis}}$ reconstruction algorithm is seeded from jet-objects reconstructed using the anti- k_t algorithm [21], with a distance parameter $R = 0.4$. Topological clusters [22] made of calorimeter cells calibrated using the Local Hadron Calibration (LC) [23] are used as an input for the jet-object algorithm. All jet-objects with $p_T \geq 10$ GeV and with $|\eta| \leq 2.5$, which corresponds to the η -coverage of the ATLAS tracking system, seed the $\tau_{\text{had-vis}}$ reconstruction algorithm².

2.3 Vertex Association

The primary vertex, defined as the vertex candidate with the highest $\sum (\text{track } p_T^2)$ [24], is not necessarily the vertex the $\tau_{\text{had-vis}}$ candidate originates from. Therefore, a dedicated vertex association method is used to identify the best vertex hypothesis for each $\tau_{\text{had-vis}}$ seed. This algorithm is known as Tau Jet Vertex Association (TJVA) and described in detail in Ref. [25]. The vertex chosen by TJVA is referred to as the tau vertex and is later used in the $\tau_{\text{had-vis}}$ track association. The direction of cell- and cluster-based variables are calculated in a coordinate system having this vertex as origin.

2.4 Tau Axis and Four-momentum

The reconstructed four-momentum of the $\tau_{\text{had-vis}}$ candidate is defined in terms of three degrees of freedom: p_T , η , and ϕ . The mass of the $\tau_{\text{had-vis}}$ candidate is defined to be zero and consequently the transverse momentum, p_T , and the transverse energy, $E_T = E \sin \theta$, are identical.

At first a barycenter is formed consisting of the sum of the four-vectors of the constituent topological clusters, assuming zero mass for each of the constituents [26]. Then the $\tau_{\text{had-vis}}$ detector axis is calculated by using clusters within $\Delta R = \sqrt{(\Delta\eta)^2 + (\Delta\phi)^2} < 0.2$ around the barycenter. The four-vectors of

²The ATLAS Coordinate System [12] is a right-handed system with the x -axis pointing to the center of the LHC ring, the y -axis pointing upwards, and the z -axis following the beam line. The spherical coordinates ϕ and θ are defined in the usual way, with the azimuthal angle, ϕ , measuring the angle in the xy -plane from the positive x -axis, increasing towards positive y . θ measures the angle from the positive z -axis, but this coordinate is often specified by the pseudorapidity, η , defined as $\eta = -\ln(\tan \frac{\theta}{2})$.

those clusters are recalculated using the tau vertex coordinate system and the vectors are summed up. The resulting axis is called the intermediate axis. The $\tau_{\text{had-vis}}$ direction (η, ϕ) is defined by this intermediate axis. Because hadronic tau decays consist of a specific mixture of charged and neutral pions, the energy scale of $\tau_{\text{had-vis}}$ candidates is adjusted independently of the jet energy scale. The reconstructed energy of $\tau_{\text{had-vis}}$ candidates is calculated to the final energy scale by a simulation-based calibration procedure using clusters, within $\Delta R < 0.2$ of the seed jet-object barycenter axis. The $\tau_{\text{had-vis}}$ energy calibration is described in detail in a separate document [27]. The final η position of the $\tau_{\text{had-vis}}$ candidate is re-calculated as a last step after all basic $\tau_{\text{had-vis}}$ variables have been calculated and after the energy calibration procedure, which takes into account clusters reconstructed in poorly instrumented regions of the calorimeter [27].

2.5 Track Association

Tracks are associated to each $\tau_{\text{had-vis}}$ candidate if they are within the *core cone*, defined as the region within $\Delta R \leq 0.2$ of the intermediate axis, and satisfy the following quality criteria:

- $p_T \geq 1 \text{ GeV}$,
- Number of pixel hits ≥ 2 ,
- Number of pixel hits + number of SCT hits ≥ 7 ,
- $|d_0| \leq 1.0 \text{ mm}$,
- $|z_0 \sin \theta| \leq 1.5 \text{ mm}$,

where d_0 is the distance of closest approach of the track to the tau vertex (explained in Section 2.3) in the transverse plane, while z_0 is the longitudinal distance of closest approach.

$\tau_{\text{had-vis}}$ candidates are classified as single or multi-prong depending on the number of tracks counted in the core cone (N_{track}). Tracks within the *isolation annulus* ($N_{\text{track}}^{\text{iso}}$), defined by $0.2 < \Delta R \leq 0.4$ of the axis of the $\tau_{\text{had-vis}}$, are also counted for variable calculations, and are required to satisfy the same track quality criteria.

2.6 Discriminating Variables

The reconstruction of $\tau_{\text{had-vis}}$ candidates provides very little rejection against the jet background to hadronically decaying tau leptons. This rejection is provided in a separate identification step, using discriminating variables that are calculated during the reconstruction. On average, jets are wider than hadronic tau decays with a given momentum. Therefore, different variables describing the shower shape in both the calorimeters and the tracking detectors are used to separate $\tau_{\text{had-vis}}$ from jets. Additionally, variables based on the number of tracks reconstructed around the candidate provide strong discriminating power. An important calorimeter shape variable is the fraction of the total tau energy contained in the centermost cone defined by $\Delta R < 0.1$, $f_{\text{core}}^{\text{corr}}$, shown in Figure 1(a). Important tracking variables are the average p_T -weighted track distance from the tau axis, R_{track} (Figure 1(b)), and, in multi-prong decays, the distance to the track furthest from the tau axis, ΔR_{max} (Figure 1(c)). Although the tau lepton decays before it reaches the tracking detector, the significance of a reconstructed secondary vertex, S_T^{flight} , provides discrimination especially in the 3-prong decay and is used for tau identification (Figure 1(d)). An in-depth description of all variables, including the ones mentioned above, can be found in Appendix A.

While variables based on tracking information are relatively pile-up robust, calorimeter-based variables are affected to a greater extent. Simultaneous pile-up events add extra energy depositions in the

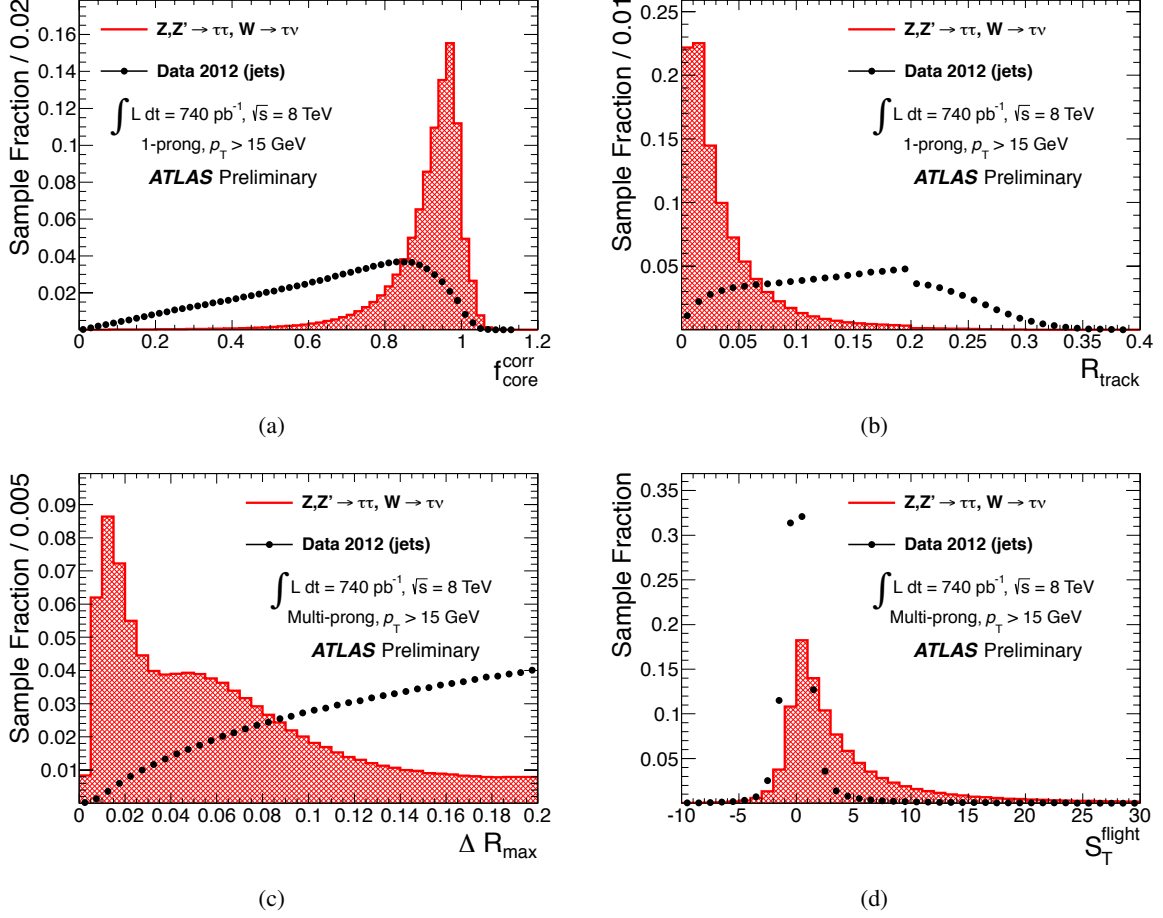


Figure 1: Distributions of a selection of jet discriminating variables for simulated $Z, Z' \rightarrow \tau\tau$ and $W \rightarrow \tau\nu$ signal samples and a jet background sample selected from 2012 data. The distributions are normalized to unity. Variable definitions can be found in Appendix A.

detector, leading to additional clusters being reconstructed close to the $\tau_{\text{had-vis}}$ candidate, or to extra energy being added to existing clusters. To decrease the pile-up dependence of the calorimeter variables, the area around the $\tau_{\text{had-vis}}$ candidate considered for their calculation has been reduced from the 2011 default value of $\Delta R < 0.4$ to $\Delta R < 0.2$. The discrimination power provided by the information contained in the isolation annulus $0.2 < \Delta R < 0.4$ is preserved by the track-based variables, e.g. the number of isolation tracks around the $\tau_{\text{had-vis}}$ candidate. To further reduce the pile-up dependence of the BDT and LLH output, a pile-up correction is applied to the calorimeter variables. It is chosen to account for the average change of the variable with respect to the number of vertices in that event (N_{vtx}). Since the pile-up dependence decreases with p_{T} , the correction is applied only on $\tau_{\text{had-vis}}$ candidates with a momentum below a certain p_{T} threshold (see also Appendix A). Other pile-up related effects can also occur due to spurious detector signals from successive bunch-crossings. The discriminating variables were therefore also tested as a function of the average number of interactions per crossing which can be used to probe such effects. It was found that the correction as a function of the number of vertices in the event was sufficient.

3 Identification of Hadronic Tau Decays

For the identification of hadronically decaying tau leptons, cut-based and multi-variate techniques are used. This section describes two approaches to discriminate $\tau_{\text{had-vis}}$ from jets: a projective likelihood method and boosted decision trees. It is followed by a description of boosted decision trees used for the rejection of electrons and a cut-based method for the rejection of muons.

3.1 Discrimination against Jets

Quark- or gluon-initiated jets are produced at high rates in the LHC and have a detector signature very similar to $\tau_{\text{had-vis}}$. Hence, they are the main source of backgrounds for hadronically decaying tau leptons. The reconstruction procedure described earlier offers little rejection against such backgrounds. A dedicated set of algorithms, referred to as the $\tau_{\text{had-vis}}$ identification (*tau ID*), is used instead for the purpose of discriminating between $\tau_{\text{had-vis}}$ and jets.

For the training of the tau ID algorithms, simulated $Z \rightarrow \tau\tau$, $W \rightarrow \tau\nu$ and $Z' \rightarrow \tau\tau$ samples are used for signal $\tau_{\text{had-vis}}$ candidates. Z' samples with a Z' mass of 250 GeV, 500 GeV, 750 GeV, 1000 GeV and 1250 GeV are used to enhance the number of high- p_T $\tau_{\text{had-vis}}$ candidates. Only well-reconstructed $\tau_{\text{had-vis}}$ candidates satisfying $|\eta| < 2.3$, $p_T > 15$ GeV are considered for the training and have to lie within $\Delta R < 0.2$ of the visible position of a true hadronic tau decay ('truth-matched'). For the visible part of the decay, the neutrino in the tau decay is ignored. The true hadronic tau decays have to satisfy the fiducial requirements $|\eta_{\text{vis}}^{\text{true}}| < 2.5$, $p_{T,\text{vis}}^{\text{true}} > 10$ GeV and $N_{\text{prong}}^{\text{true}} = 1$ or 3. In the tau ID algorithms, three groups of $\tau_{\text{had-vis}}$ candidates are used:

- *1-prong* candidates with one reconstructed track matched to a true τ_{had} with one charged hadron,
- *3-prong* candidates with three reconstructed tracks matched to a true τ_{had} with three charged hadrons,
- *multi-prong* candidates with two or three reconstructed tracks matched to a true τ_{had} with three charged hadrons.

For the QCD backgrounds, a jet-enriched data sample from 2011 (BDT) and 2012 (LLH) is used for the training. For the validation of both methods, data from early 2012 are taken. The background $\tau_{\text{had-vis}}$ candidates also have to fulfill $|\eta| < 2.3$ and $p_T > 15$ GeV. The three groups of candidates are defined in accordance to the above, requiring one reconstructed track (1-prong), three reconstructed tracks (3-prong) and two or three reconstructed tracks (multi-prong).

The reconstruction and identification efficiency for signal events is defined as the number of truth-matched $\tau_{\text{had-vis}}$ candidates passing identification divided by all true hadronic tau decays. The background efficiency is defined as the number of background $\tau_{\text{had-vis}}$ candidates passing identification divided by the number of all background $\tau_{\text{had-vis}}$ candidates. Often, the inverse of the background efficiency is plotted. Efficiencies are plotted in bins of $\tau_{\text{had-vis}}$ variables or event variables (e.g. p_T , η , N_{vtx}). The binning is then applied to both the numerator and the denominator, so that both reconstructed and true $\tau_{\text{had-vis}}$ are within the same kinematic region. In 1-prong (3-prong) efficiencies $\tau_{\text{had-vis}}$ candidates with one (three) reconstructed tracks and true τ_{had} with one (three) charged hadrons are considered. The multi-prong efficiency is defined as the 3-prong efficiency, but considering two or three reconstructed tracks.

3.1.1 BDT ID

The identification with boosted decision trees (BDT tau ID) has been described previously in detail [28]. Two BDTs are trained separately for 1-prong and 3-prong $\tau_{\text{had-vis}}$ candidates, using the TMVA pack-

Variable	LLH tau ID		BDT tau ID		e-veto	muon veto
	1-prong	3-prong	1-prong	3-prong	1-prong	1-prong
$f_{\text{core}}^{\text{corr}}$	•	•	•	•	•	
$f_{\text{track}}^{\text{corr}}$	•	•	•	•	•	
f_{track}					•	•
R_{track}	•	•	•	•	•	
$S_{\text{lead track}}$	•		•			
$N_{\text{track}}^{\text{iso}}$	•		•			
ΔR_{max}		•		•		
$S_{\text{T}}^{\text{flight}}$		•		•		
m_{tracks}		•		•		
f_{EM}					•	•
f_{HT}					•	
$E_{\text{T,max}}^{\text{strip}}$					•	
$f_{\text{HCAL}}^{\text{leadtrk}}$					•	
$f_{\text{ECAL}}^{\text{leadtrk}}$					•	
f_{PS}					•	
$f_{\text{EM}}^{\pi^{\pm}}$					•	
f_{iso}					•	
R_{Had}					•	

Table 1: Comparison of variables used by the $\tau_{\text{had-vis}}$ identification algorithms: projective likelihood identification (LLH tau ID), boosted decision tree identification (BDT tau ID), boosted decision tree based electron veto (e-veto) and cut based muon veto (muon veto). Variable definitions can be found in Appendix A.

age [29]. Compared to the previous algorithm, a smaller number of variables is used for the BDT training, in order to find a more pile-up-robust variable set. The variables are listed in Table 1 and defined in Appendix A. The BDT trained with 3-prong candidates is used for classifying all $\tau_{\text{had-vis}}$ candidates with two or more tracks. Three working points — *loose*, *medium*, *tight* — are defined, corresponding to target efficiencies of 70%, 60% and 40% for 1-prong and 65%, 55% and 35% for multi-prong $\tau_{\text{had-vis}}$ candidates, respectively. The 1-prong target efficiencies have been adjusted in comparison to 2011, in order to account for the efficiency of the electron veto (see Section 3.2). In most physics analyses, this veto is applied on top of tau ID.

To compensate for the p_T dependence of the BDT in the low-momentum region, the working points are determined in bins of true visible p_T . Using the $Z \rightarrow \tau\tau$ sample, 30 bins are chosen with an equal number of $\tau_{\text{had-vis}}$ candidates. The cut on the BDT score to meet the target efficiency is estimated separately for 1-prong and multi-prong candidates. The thresholds are then interpolated between bin centers. They are constant above approximately 50 GeV. The efficiencies as a function of the momentum are shown in Figures 2(a) – 2(d). The sudden change of the efficiency at 80 GeV is due to a different pile-up correction applied to one of the calorimeter variables below and above this threshold (see Section 2.6). The BDT trained with the revised list of variables is approximately independent of the pile-up conditions, as shown in Figures 2(e) – 2(h). Therefore, no binning or flattening in the number of vertices per event is performed.

3.1.2 LLH ID

The basic procedure of $\tau_{\text{had-vis}}$ identification with a projective likelihood function has been described previously [30]. The same set of variables as for the BDT ID is used to create one-dimensional probability density functions (PDFs), as shown in Table 1. The PDFs are binned in the number of tracks associated with the $\tau_{\text{had-vis}}$ candidate (1-prong and 3-prong) and in the transverse momentum of the $\tau_{\text{had-vis}}$, using the p_T bins < 45 GeV, 45–100 GeV and > 100 GeV. An additional binning in the number of vertices per event, as it was used in Ref. [30], was omitted, since corrections to account for the pile-up dependence of variables are applied directly on the input variables. Calculating the final likelihood score requires a linear interpolation at the borders of the p_T bins. For each border, a symmetric window of $[-10, +10]$ GeV is used, except for the 100 GeV border for 1-prong $\tau_{\text{had-vis}}$, where an asymmetric window of $[-30, +60]$ GeV is used.

To be consistent with the BDT identification, the same working point definitions for *loose*, *medium*, *tight* were used, corresponding to target efficiencies of 70%, 60% and 40% for 1-prong and 65%, 55% and 35% for multi-prong $\tau_{\text{had-vis}}$ candidates, respectively. To consider the p_T dependence of the likelihood score, the likelihood score cuts were determined as a function of true visible tau p_T , to achieve approximately flat efficiencies in p_T for each working point and each number of associated tracks classification. The efficiencies for signal MC and background di-jet samples are presented in Figure 3.

3.1.3 Performance

Figure 4 shows the inverse background efficiency as a function of signal efficiency for the two jet discrimination algorithms BDT and LLH. Both methods have compatible performance. Background rejection factors of 10–40 for signal efficiencies of 70% are achieved, going up to 500 for 35% signal efficiency. One should note that in practice, the background efficiency will depend on the event selection, as it depends on the kinematics of the candidates considered and the type of partons that initiated the jets. The upper bound on the signal efficiency is subject to the efficiency-loss due to the track selection during $\tau_{\text{had-vis}}$ reconstruction.

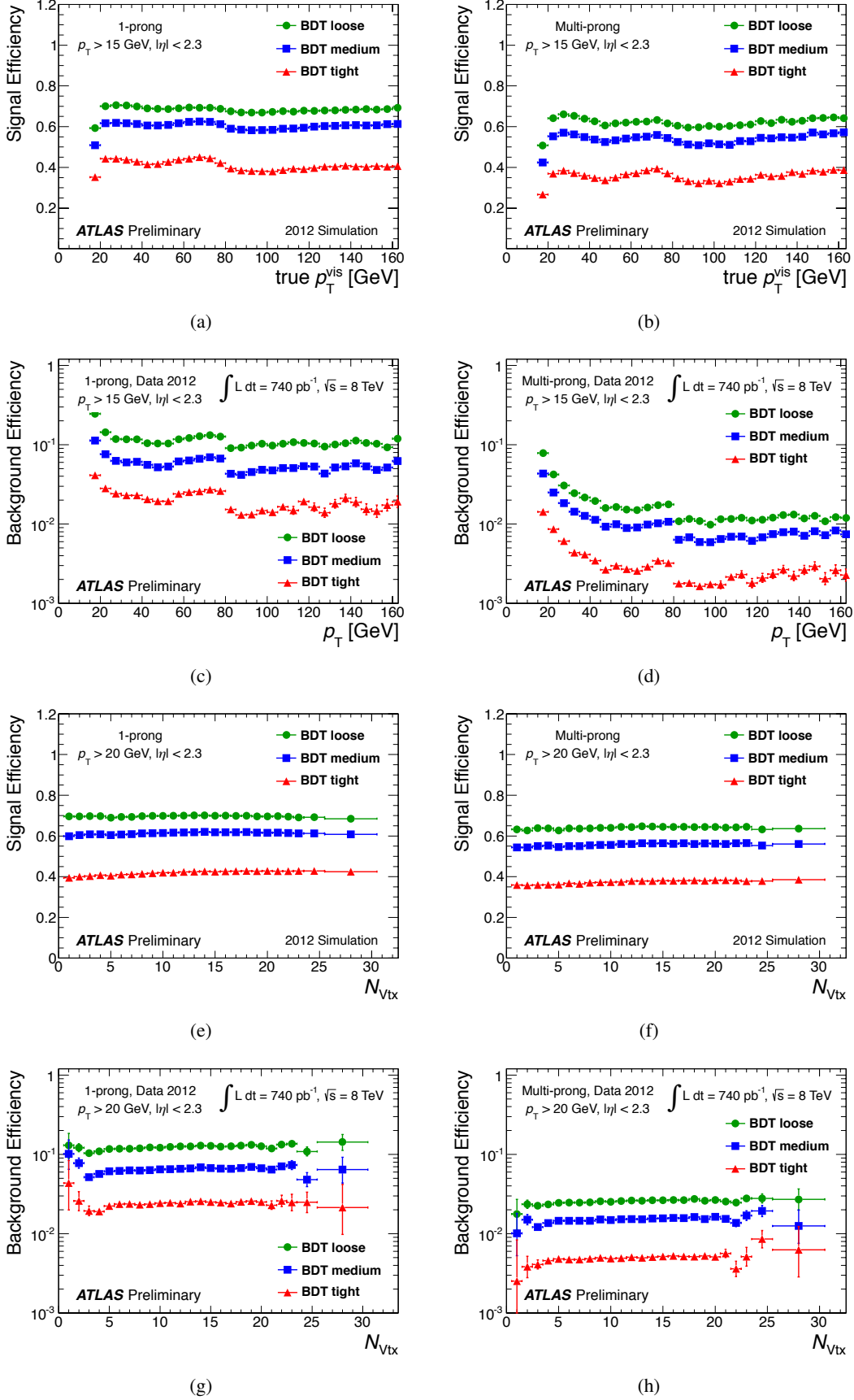


Figure 2: Signal and background efficiencies for 1-prong (left) and multi-prong (right) $\tau_{\text{had-vis}}$ candidates for the three working points of the BDT $\tau_{\text{had-vis}}$ ID as a function of true visible tau p_T for signal candidates ((a) – (b)) and reconstructed p_T for background candidates ((c) – (d)) and number of vertices ((e) – (h)). The efficiencies were obtained using $Z \rightarrow \tau\tau$, $Z' \rightarrow \tau\tau$ and $W \rightarrow \tau\nu$ simulated samples for signal and multi-jet events from data for background.

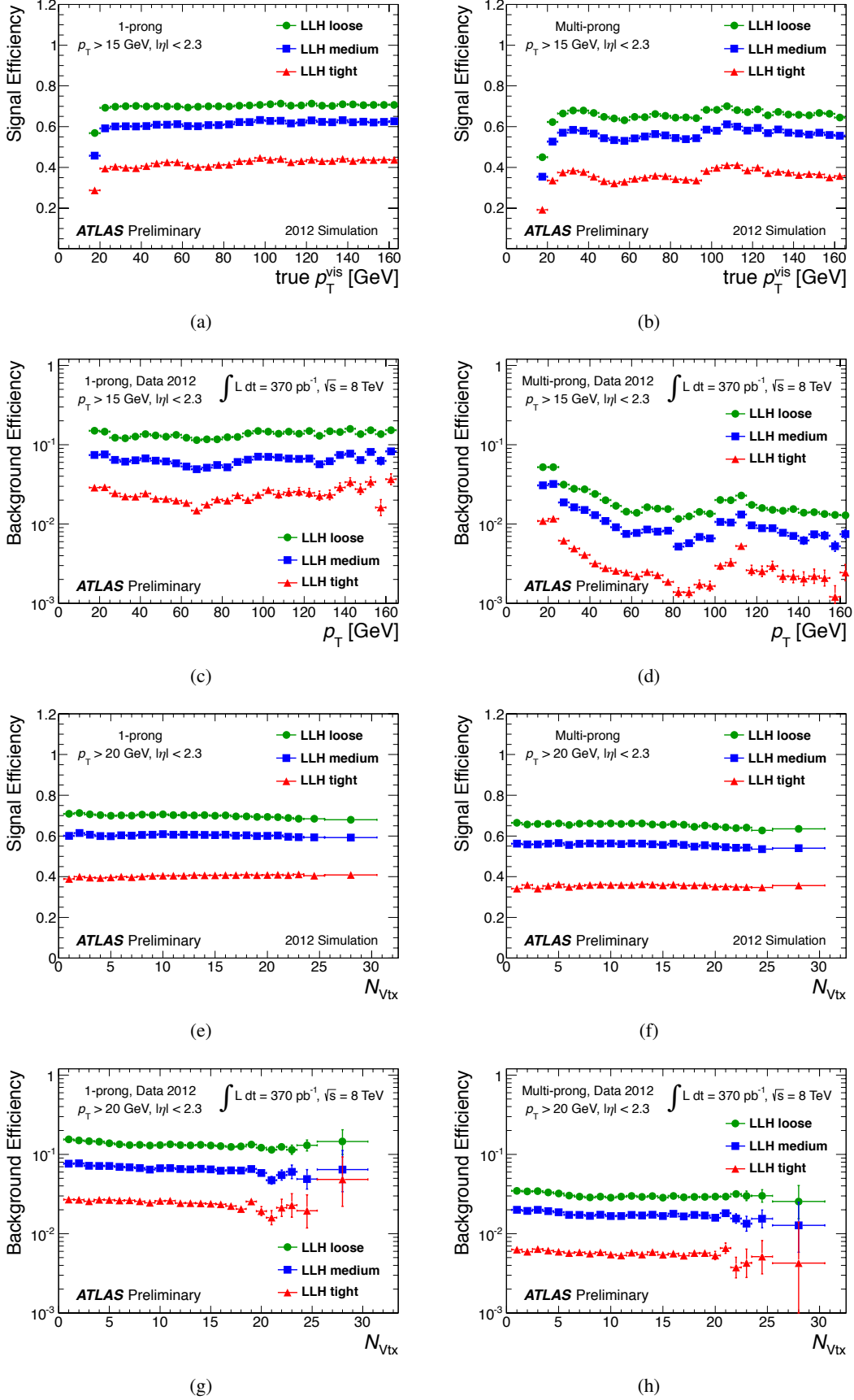


Figure 3: Signal and background efficiencies for 1-prong (left) and multi-prong (right) $\tau_{\text{had-vis}}$ candidates for the three working points of the LLH τ_{ID} as a function of true visible tau p_T for signal candidates ((a) – (b)) and reconstructed p_T for background candidates ((c) – (d)) and number of vertices ((e) – (h)). The efficiencies were obtained using $Z \rightarrow \tau\tau$, $Z' \rightarrow \tau\tau$ and $W \rightarrow \tau\nu$ simulated samples for signal and multi-jet events from data for background.

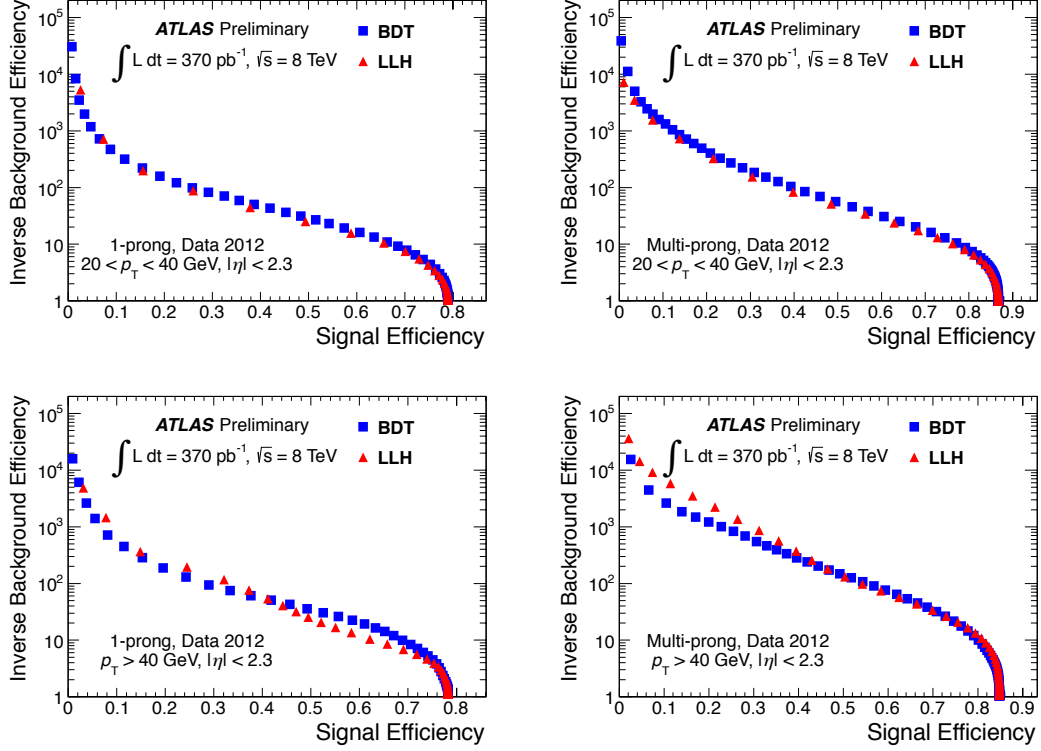


Figure 4: Inverse background efficiencies as a function of signal efficiency for 1-prong (left) and multi-prong (right) candidates, in low (top) and high (bottom) p_T ranges, for the two tau ID methods BDT and LLH. The signal efficiencies were obtained using $Z \rightarrow \tau\tau$, $Z' \rightarrow \tau\tau$ and $W \rightarrow \tau\nu$ simulated samples and the inverse background efficiencies from data multi-jet events.

3.2 Discrimination against Electrons

This section gives an overview of the electron veto discriminant used in the identification of hadronically decaying tau leptons. The characteristic signature of 1-prong $\tau_{\text{had-vis}}$ can be mimicked by electrons. This creates a significant background contribution after all the jet related backgrounds are suppressed via kinematic, topological and $\tau_{\text{had-vis}}$ identification criteria. Despite the similarities of the $\tau_{\text{had-vis}}$ and electron signatures, there are several properties that can be used to discriminate between them. The most useful examples of such properties are the emission of transition radiation of the electron track and the longer and wider shower produced by the hadronic tau decay products in the calorimeter, compared to the one created by an electron. The full list of variables used in the electron veto is shown in Table 1. These properties are used to define $\tau_{\text{had-vis}}$ identification discriminants specialized in the rejection of electrons mis-identified as hadronically decaying tau leptons. In 2012 the only method for this uses boosted decision trees, using the TMVA package [29]. Recent studies have shown that 3-prong $\tau_{\text{had-vis}}$ can also be mimicked by electrons. This has not been considered in this note, but will be investigated in future electron veto studies.

The electron veto BDT (e-veto BDT) is optimized using simulated $Z \rightarrow \tau\tau$ events for the signal and $Z \rightarrow ee$ events for the background. The signal candidates are required to be matched to true 1-prong hadronic tau decays, while background candidates are matched to true electrons. In addition, both signal and background candidates have to satisfy $p_T > 20 \text{ GeV}$ and BDT *loose* tau ID. Candidates overlapping with reconstructed electrons are removed.

The e-veto BDT was trained for different η regions: $|\eta| < 1.37$, $1.37 < |\eta| < 2.0$, $2.0 < |\eta| < 2.3$ and

$|\eta| > 2.3$. Slightly different sets of variables were used in each training region. The signal vs. background efficiencies for the different η regions are shown in Figure 5.

The performance of the e-veto BDT was tested for dependences on a number of different variables: the number of inelastic pp interactions per event μ , the transverse momentum p_T and the pseudorapidity η . The dependence on η and μ was not considered significant enough to warrant a dedicated flattening of the signal efficiency with respect to these variables. The dependence on p_T was such that a sliding cut on the e-veto BDT score was used when implementing the three efficiency working points *loose*, *medium* and *tight*. These working points were chosen to yield signal efficiencies of 95%, 85% and 75%, respectively. The dependence of the efficiency of the electron veto on μ , p_T and η is shown in Figure 6.

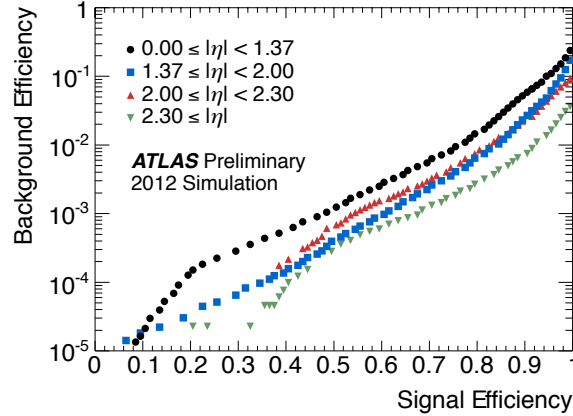


Figure 5: Background efficiency as a function of signal efficiencies of the electron veto for each of the different η regions. The efficiencies are obtained using simulated $Z \rightarrow \tau\tau$ events for signal and simulated $Z \rightarrow ee$ events for background.

3.3 Discrimination against Muons

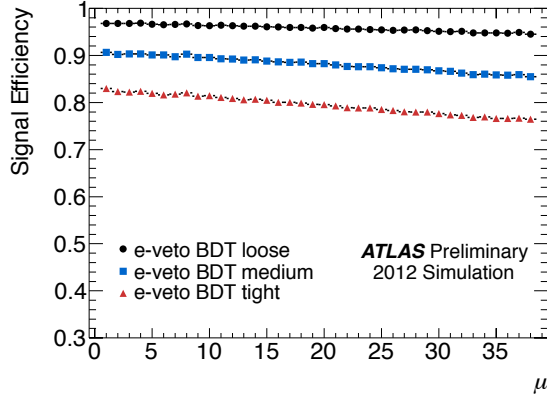
As minimum ionizing particles, muons are unlikely to deposit enough energy in the calorimeters to be reconstructed as a $\tau_{\text{had-vis}}$ candidate. However, when a sufficiently energetic cluster in the calorimeter is associated with a muon, the muon track and the calorimeter cluster together may be mis-identified as a $\tau_{\text{had-vis}}$. In 2011, a simple cut-based discriminant was optimized to distinguish these muons from true hadronic tau decays. This has been re-tuned and improved for 2012.

The most effective means of rejecting fake $\tau_{\text{had-vis}}$ from muons is to use the default muon reconstruction algorithms: if a $\tau_{\text{had-vis}}$ candidate overlaps geometrically with a reconstructed muon it is not considered by analyses. This primarily leaves the following cases:

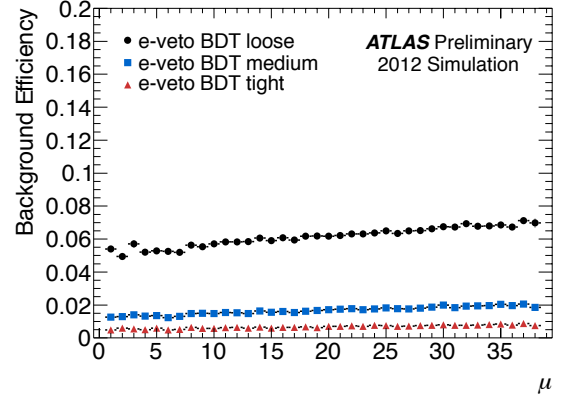
- The muon has passed through an inefficient region of the Muon Spectrometer and was not reconstructed.
- The muon has deposited enough energy in the calorimeter that its track is skewed, and reconstruction in the Muon Spectrometer fails.
- The muon was of very low energy, and was stopped in the calorimeter.

In the first case, the low-efficiency regions occur at very low $|\eta|$, where there is a gap in muon coverage to allow access to the inner detector, and in the transition region between barrel and end-cap³ in the detector side with $\eta > 0$. The increased rate of muon fakes in these regions can be seen in Figure 7(a).

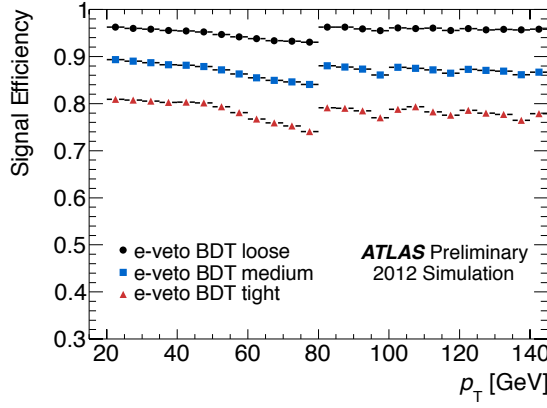
³Specifically, for the purpose of this veto the low-efficiency region is defined as $|\eta| < 0.1$ or $1.15 < \eta < 1.3$.



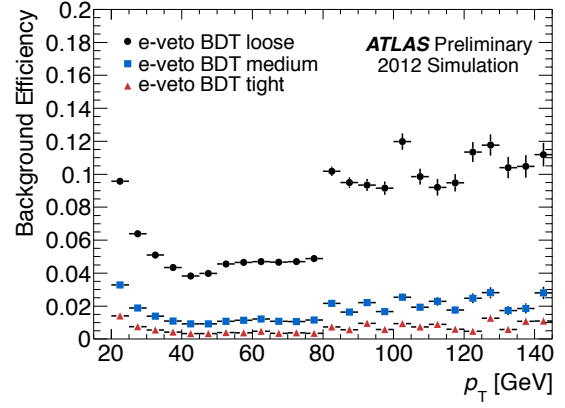
(a)



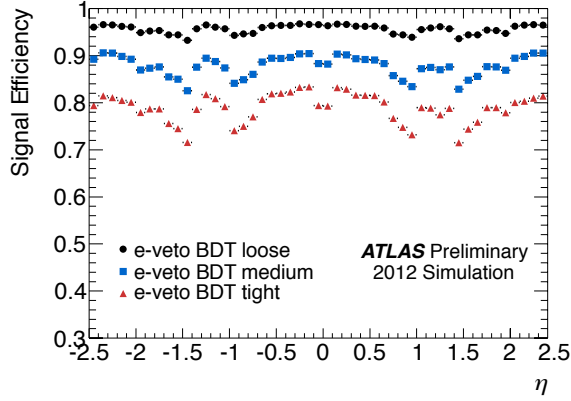
(b)



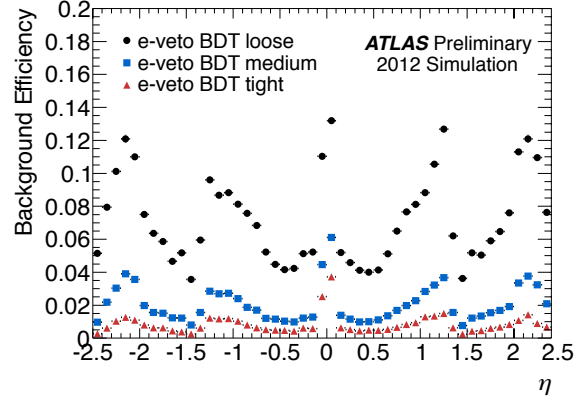
(c)



(d)



(e)



(f)

Figure 6: Signal (left) and background (right) efficiencies for the three BDT e -veto working points as a function of μ , p_T and η , with μ being the average number of pile-up interactions per bunch crossing. The efficiencies are obtained using 1-prong $\tau_{\text{had-vis}}$ candidates from simulated $Z \rightarrow \tau\tau$ events for signal and simulated $Z \rightarrow ee$ events for background.

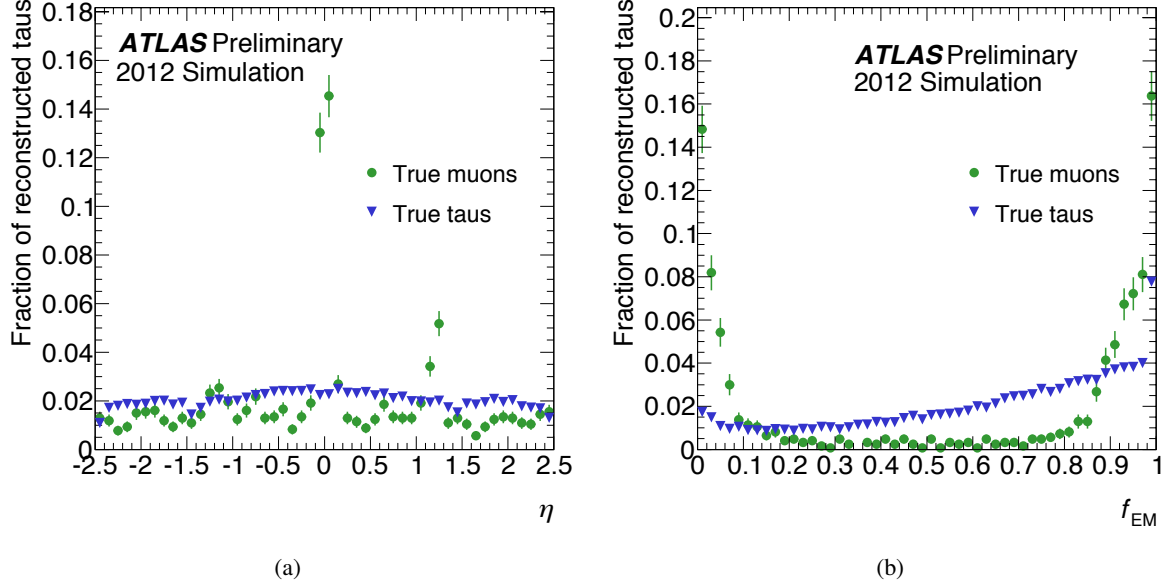


Figure 7: (a) Pseudorapidity η of $\tau_{\text{had-vis}}$ candidates in simulation matched to true muons and true τ_{had} , after removing candidates which overlap with a reconstructed muon. The effect of inefficient muon reconstruction in certain regions can be seen. (b) Electromagnetic fraction f_{EM} of $\tau_{\text{had-vis}}$ candidates in simulation matched to true muons and true τ_{had} .

Muons which have deposited significant energy in the calorimeter are likely to have done so mostly in the hadronic calorimeter, resulting in $\tau_{\text{had-vis}}$ candidates with an unusually low electromagnetic fraction f_{EM} (see Appendix A for the variable definition). Additionally, for these muons the track momentum may be higher than the calorimeter energy, which is also true of muons that overlap coincidentally with some other calorimeter deposit. Finally, the very low-energy muons must overlap with some other calorimeter energy to pass the $\tau_{\text{had-vis}}$ reconstruction (perhaps final state radiation from the same muon), and are therefore characterized by a high electromagnetic fraction and low track momentum fraction. Figure 7(b) shows the distribution of the electromagnetic fraction for $\tau_{\text{had-vis}}$ candidates seeded by true muons and by true tau leptons.

To optimize the muon veto, simulated muons from $Z \rightarrow \mu\mu$ events and hadronic tau decays from $Z \rightarrow \tau\tau$ events were used. Regions of low and high electromagnetic fraction were defined, and a cut on the track momentum fraction is applied in each, with separate region definitions and cuts for $\tau_{\text{had-vis}}$ in the low-muon-efficiency areas.

The resulting efficiency is better than 96% for true τ_{had} , with a reduction of muon fakes around 40%. However the performance can vary depending on the $\tau_{\text{had-vis}}$ identification and muon overlap removal in use.

4 Measurements of the Hadronic Tau Identification Efficiency Scale Factors

As described in the last section, the various ATLAS $\tau_{\text{had-vis}}$ identification algorithms have been tuned using simulations to provide specific efficiency working points. It is important to verify that these identification algorithms perform comparably in both the predictions from simulated samples and in data. This is done by measuring the identification efficiency for reconstructed $\tau_{\text{had-vis}}$ candidates directly in data.

By comparing these results to the same performance figures in simulated event samples, scale factors are derived. These scale factors are then used in analyses to account for the differences between data and simulation due to modeling of the input variables. The measurement of these scale factors is the focus of this section. No scale factors are provided for the efficiency in rejecting backgrounds, as this quantity is too sensitive to the final state being studied; dedicated studies of the background efficiency should be performed on a per-analysis basis to ensure proper treatment of the various dependences.

The ‘tag-and-probe’ approach chosen consists of selecting events with real tau leptons in their final state, and extracting a measure of the identification efficiencies directly from the number of reconstructed $\tau_{\text{had-vis}}$ before and after identification algorithms are applied. In practice, it is impossible to obtain a pure sample of hadronically decaying tau leptons, and therefore, backgrounds must be taken into account. To estimate the number of background events, a variable with good separation potential is chosen. A fit is then performed using the expected distributions in this variable (*templates*) for both signal and backgrounds. The fit has to be performed multiple times: once before any identification is used and once after each identification algorithm. The real number of hadronic tau decays in data is then obtained from the fitted signal template. To measure the tau ID efficiency for data, ϵ_{data} , the number of real $\tau_{\text{had-vis}}$ after tau ID is divided by the number of real $\tau_{\text{had-vis}}$ before tau ID. The uncertainties on the efficiency measurement are estimated by recalculating the efficiency using systematically altered templates. For the efficiency in simulated samples, $\epsilon_{\text{simulation}}$, the number of tau leptons before and after tau ID is taken directly from truth-matched $\tau_{\text{had-vis}}$ candidates.

The scale factors provided represent:

$$\text{SF} = \frac{\epsilon_{\text{data}}}{\epsilon_{\text{simulation}}} . \quad (1)$$

The uncertainty on the scale factors is propagated from the uncertainty of the efficiency measurement in data. The definition of the efficiencies measured varies based on the selection criteria on the $\tau_{\text{had-vis}}$ candidates used in the different channels. These scale factors therefore account for the differences between data and simulation due to the modeling of the input variables for the identification algorithms.

This measurement is repeated in different final states, aiming at different underlying physics processes where hadronically decaying tau leptons are produced. Three processes are chosen: $Z \rightarrow \tau_{\text{lep}}\tau_{\text{had}}$, $W \rightarrow \tau_{\text{had}}\nu_{\tau}$, and $t\bar{t} \rightarrow \tau_{\text{had}} + \text{jets}$. The $Z \rightarrow \tau_{\text{lep}}\tau_{\text{had}}$ channel is chosen as the main measurement as it offers the highest precision due to the low associated backgrounds. This channel offers coverage of the range $20 < p_T < 50$ GeV. The measurement in the $W \rightarrow \tau_{\text{had}}\nu_{\tau}$ channel is used as a cross-check, and offers coverage in the $20 < p_T < 60$ GeV regime. Finally, the $t\bar{t} \rightarrow \tau_{\text{had}} + \text{jets}$ channel offers an alternative measurement in the higher kinematic regime of $40 < p_T < 100$ GeV. This channel also offers a busier event environment than the other channels.

4.1 Fitting Methodology

To determine the number of signal and background events in the chosen topologies, a fit to data is used. The signal and the background are modeled with templates, obtained from either simulations or data-driven techniques. The variable chosen for the fit is the extended track multiplicity associated to the $\tau_{\text{had-vis}}$ candidate as it provides good separation between the signal and the backgrounds.

As real $\tau_{\text{had-vis}}$ tend to be more collimated for a given p_T with respect to the jets which mimic them, the $\tau_{\text{had-vis}}$ reconstruction algorithm associates tracks to the candidate within a narrow cone of $\Delta R \leq 0.2$ with respect to the $\tau_{\text{had-vis}}$ direction; this definition is referred to as N_{track} . However, for gluon- and quark-initiated jets, the region outside of this outer cone is still likely populated with numerous tracks. Therefore, to improve the separation between real $\tau_{\text{had-vis}}$ and mis-identified jets, it is useful to extend the region in which tracks are counted. To do this, tracks outside of the core cone (outer tracks) are counted according to the algorithm described in Ref. [25]. This algorithm compares outer tracks to inner tracks,

using both ΔR and p_T to determine the ‘significance’ of each outer track (ie. whether its p_T is significant enough to ensure that it comes from the same object and not from underlying events or pile-up). The same definition is adopted for all channels. Outer tracks are taken in the $0.2 < \Delta R \leq 0.6$ annulus around the core cone and are required to have $p_T > 500$ MeV. For a given outer track, the distance parameter D^{outer} is separately calculated with respect to all inner tracks; if any of the calculated distances satisfies the requirement $D^{\text{outer}} < 4.0$, the outer track is included. For an inner and outer track pair, the distance parameter is defined as:

$$D^{\text{outer}} = \frac{p_T^{\text{inner}}}{p_T^{\text{outer}}} \times \Delta R(\text{inner, outer}) . \quad (2)$$

This particular counting algorithm is referred to as p_T -correlated track counting, and the resulting variable as $N_{\text{track}}^{\text{corr}}$. For the fit, the sum of core tracks and p_T -correlated tracks is used, referred to as extended track multiplicity $N_{\text{track}}^{\text{c+c}}$. It is important to note that different templates must be obtained for the fits before and after identification criteria are applied, as the identification algorithms distort the distributions of the extended track multiplicity.

4.2 Measurement with $Z \rightarrow \tau_{\text{lep}}\tau_{\text{had}}$ Events

4.2.1 Event Selection

In this section, hadronic tau decays from $Z \rightarrow \tau_{\text{lep}}\tau_{\text{had}}$ events are considered. To isolate such events with a high purity, a tag-and-probe selection is used. Events are selected requiring the presence of a light lepton (electron or muon) tag, and then searching for the probe tau decaying hadronically. The selection requirements for both the electron and muon channel are listed in Table 2.

The very loose requirement on the tau ID BDT score of the probe $\tau_{\text{had-vis}}$ candidate has been proven to strongly suppress quark- and gluon-initiated jets while introducing a negligible bias on the signal (less than 1% rejected real $\tau_{\text{had-vis}}$ in simulated events), as shown in Ref. [25]. The upper threshold on the light tag lepton p_T , and the last three event topology cuts are designed to reduce backgrounds from $W + \text{jets}$ events. The extended track multiplicity distribution after the selection has been applied, and before and after identification criteria have been applied, can be found in Figures 8 and 9. In these figures, the multi-jet background is not included as it is later determined using data-driven techniques; this background accounts for most of the difference between the data and simulation. In order to study the η dependence of the scale factors, $\tau_{\text{had-vis}}$ candidates in the barrel and end-cap regions are studied separately.

4.2.2 Backgrounds and Templates

The signal is modeled taking the extended track multiplicity distribution predicted by $Z \rightarrow \tau_{\text{lep}}\tau_{\text{had}}$ events simulated using PYTHIA. To obtain the signal shape, the probe is matched to a true hadronically decaying tau lepton. The dominant background shape is modeled by the data distribution taken from a control region defined requiring the tag and the probe to have the same charge (SS region). This background is composed of quark- or gluon-initiated jets which are produced either in association with vector bosons (electroweak backgrounds), or in pure strong interactions (multi-jet events). The data shape taken from the same-sign region models both of these two components. Differences in the background shape between the signal (OS) region and SS regions due to different quark/gluon compositions are strongly reduced by selecting candidates with tau ID BDT score > 0.3 , as shown in Ref. [25]. Differences between the OS and SS regions are taken into account as a systematic uncertainty as is discussed in Section 4.2.3.

	<i>Electron Channel</i>	<i>Muon Channel</i>
Trigger	one isolated electron with $E_{\text{T}} > 24$ GeV	one isolated muon with $p_{\text{T}} > 20$ GeV (tighter isolation) or 24 GeV (looser isolation)
<i>Light tag lepton requirements</i>		
lepton	identified electron	identified muon
p_{T}	$25 \text{ GeV} < p_{\text{T}}^e < 40 \text{ GeV}$	$22 \text{ GeV} < p_{\text{T}}^\mu < 40 \text{ GeV}$
η	$ \eta^e < 1.37$ or $1.52 < \eta^e < 2.47$	$ \eta^\mu < 2.4$
Isolation	sum of E_{T} in $\Delta R < 0.2$ less than 8% of p_{T}^e	sum of E_{T} in $0.05 < \Delta R < 0.2$ less than 4% of p_{T}^μ
	no other tracks with $p_{\text{T}} > 1$ GeV within $\Delta R < 0.4$	
<i>Probe $\tau_{\text{had-vis}}$ requirements</i>		
p_{T}	$p_{\text{T}}^{\tau_{\text{had-vis}}} > 20$ GeV	
η	$ \eta^{\tau_{\text{had-vis}}} < 2.47$	
N_{track}	$N_{\text{track}} > 0$	
tau ID	tau ID BDT score > 0.3	
e -veto	<i>loose</i> if $N_{\text{track}} = 1$	<i>loose</i> if $N_{\text{track}} = 1$
<i>Event and topology requirements</i>		
	One primary vertex with at least 4 associated tracks No other reconstructed leptons in the event light lepton (l) and $\tau_{\text{had-vis}}$ must satisfy $42 \text{ GeV} < m_{\text{vis}}(l, \tau_{\text{had-vis}}) < 82 \text{ GeV}$ light lepton (l) and $\tau_{\text{had-vis}}$ must have opposite charge $m_{\text{T}} = \sqrt{2p_{\text{T}}^l \cdot E_{\text{T}}^{\text{miss}}(1 - \cos \Delta\phi(l, E_{\text{T}}^{\text{miss}}))} < 50 \text{ GeV}$ $\cos \Delta\phi(l, E_{\text{T}}^{\text{miss}}) + \cos \Delta\phi(\tau_{\text{had-vis}}, E_{\text{T}}^{\text{miss}}) > -0.15$ $\Delta\phi(\tau_{\text{had-vis}}, l) > 2.4$	

Table 2: Event selection requirements for $Z \rightarrow \tau_{\text{lep}}\tau_{\text{had}}$ events in the electron and muon channels.

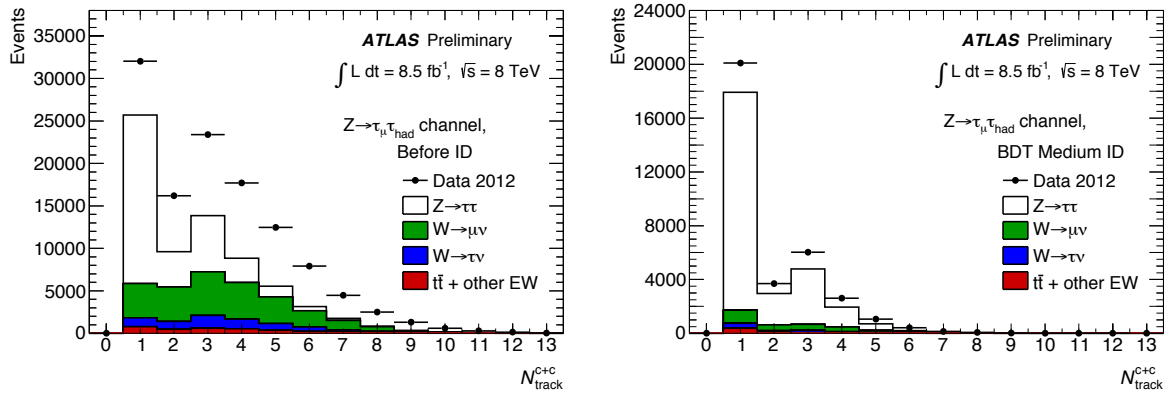


Figure 8: $Z \rightarrow \tau_\mu\tau_{\text{had}}$ channel: extended track multiplicity of the $\tau_{\text{had-vis}}$ candidate before tau ID (left) and after BDT medium tau ID (right) in the signal region. The multi-jet contribution is not shown in the plots.

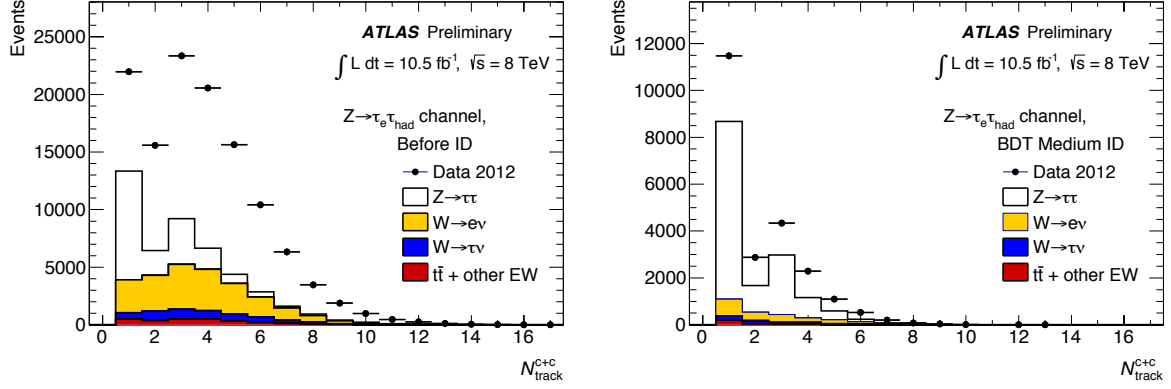


Figure 9: $Z \rightarrow \tau_e \tau_{\text{had}}$ channel: extended track multiplicity of the $\tau_{\text{had-vis}}$ candidate before tau ID (left) and after BDT medium tau ID (right) in the signal region. The multi-jet contribution is not included in the plots.

An additional background shape is required to account for the electron contamination. For the muon channel, this small background contribution is modeled taking the predicted shape from simulations with candidates which are not matched to true τ_{had} in $Z \rightarrow \tau\tau$ events. For the electron channel, this background is dominated by $Z \rightarrow ee$ events, and the shape is taken directly from the simulated events. In both channels, the electron contribution is not fitted along with the signal and the main background; instead, its normalization is fixed to the value predicted by the simulation. To measure both the 1-prong and multi-prong efficiencies, the fit is performed modeling the signal with two templates, one for 1-prong $\tau_{\text{had-vis}}$ and the other for multi-prong $\tau_{\text{had-vis}}$. These templates are obtained by imposing a requirement on the number of tracks associated to the $\tau_{\text{had-vis}}$ candidate in the core cone, N_{track} , which has to be exactly one for 1-prong $\tau_{\text{had-vis}}$ and more than one for multi-prong $\tau_{\text{had-vis}}$.

4.2.3 Systematic Uncertainties

To evaluate the systematic uncertainties, the fit is repeated with altered templates which take into account various systematic effects. This is done for the signal and for each background template. The difference with respect to the nominal fit result is then accounted for as a systematic uncertainty. Due to lack of statistics in the signal samples which are altered for systematic effects, the following procedure is adopted: the nominal template (PYTHIA) and the systematically altered templates are obtained without applying the full tag-and-probe selection listed in Table 2. This is done in order to increase statistics by recovering signal events which would have failed to fulfill the tag-and-probe requirements. This relies on the simple assumption that the systematics on the modeling of the probe $\tau_{\text{had-vis}}$ are uncorrelated with the tag selection (requirements on the muon/electron and event topology). The ratio of the systematically altered templates and nominal PYTHIA template before tag-and-probe selection, binned in extended track multiplicity N_{track}^{c+c} , is then taken to rescale the nominal template after the full tag-and-probe selection. The template obtained is used to repeat the fit. Systematics are evaluated on the modeling of the signal template in simulation, and account for the choice of generator, hadronic shower model, fragmentation model parameters and detector geometry. The systematic associated with the hadronic shower model is measured testing two models, FTFP_BERT and QGSP, and taking the largest systematic variation between the two. A more detailed description of the signal systematics can be found in Ref. [25].

The default pile-up reweighting scheme includes a scale factor which is tuned such that the simulated samples describe accurately the distribution of the number of vertices in data. By changing this scale factor up and down by the recommended uncertainty, two alternative signal templates are obtained. The

difference between the fit results obtained with the alternative and nominal templates is assigned as the uncertainty due to pile-up, and is found to be very small.

For the main background systematic uncertainty, the background shape is altered in a similar way as described in Ref. [25]. Same-sign electroweak and $t\bar{t}$ background events taken from simulation (‘MC’) are subtracted from the same-sign region in data. The opposite-sign contribution from these backgrounds is then added instead. This is to correct for possible biases in the template shape due to the charge distribution for these backgrounds. In addition to this, the shape obtained after the same-sign subtraction is rescaled in the extended track multiplicity bins by the ratio of the number of events between the opposite-sign and same-sign anti-isolated control regions, defined by inverting the selection on calorimeter isolation on the light lepton. This region is multi-jet dominated, and this serves to estimate the effect of the charge distribution in multi-jet events. The altered background shape can be expressed as:

$$\text{BKG}_{\text{OS-SS}}(N_{\text{track}}^{c+c}) = (\text{data}_{\text{SS}}(N_{\text{track}}^{c+c}) - \sum_i^{\text{all MC}} \text{MC}_{i,\text{SS}}(N_{\text{track}}^{c+c})) \frac{N_{\text{anti iso}}^{\text{OS}}}{N_{\text{anti iso}}^{\text{SS}}}(N_{\text{track}}^{c+c}) + \sum_i^{\text{all MC}} \text{MC}_{i,\text{OS}}(N_{\text{track}}^{c+c}) .$$

This uncertainty is referred to as the OS-SS systematic. The nominal template for the dominant background before and after $\tau_{\text{had-vis}}$ identification is plotted together with the systematically altered template in Figures 10 and 11.

Each systematically altered template, for the signal or background systematics, is obtained separately for the overall measurement and in each pseudorapidity bin. The final uncertainties calculated using altered templates are symmetrized.

The systematic uncertainty associated to the electron contamination is evaluated repeating the fit twice, varying the fixed normalization of the electron template by 100%. The uncertainty is then evaluated as the difference between the results of these two fits.

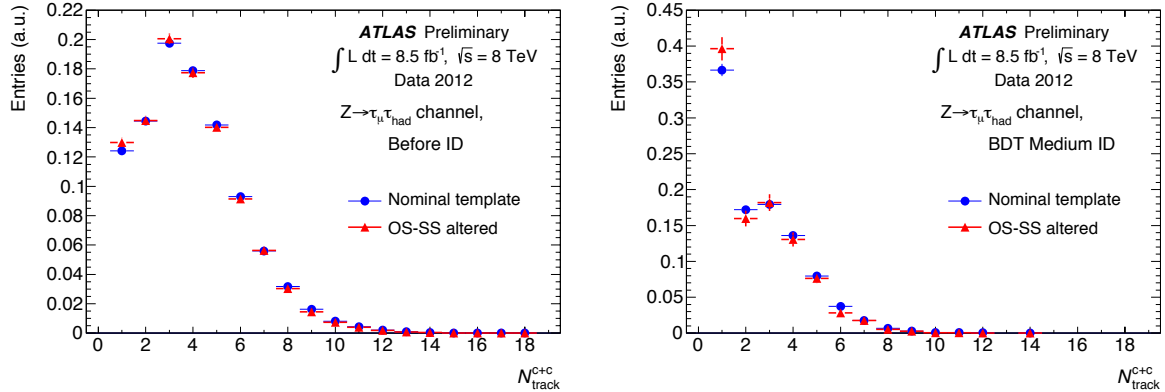


Figure 10: $Z \rightarrow \tau_{\mu}\tau_{\text{had}}$ channel: nominal background template from data in same-sign control region and systematically altered background template before tau ID (left) and after BDT medium tau ID (right). The distribution shown is the sum of core and p_{T} -correlated tracks.

4.2.4 Fit and Results

The fit procedure and the fit parameters are described in detail in Ref. [25]. Even with the introduction of the electron template, the fitting procedure does not change with respect to the given reference as the normalization of this contribution is fixed. In contrast with what is described in Ref. [25], the 1-prong and multi-prong normalizations are not left free to vary independently in the fit before identification, in order to avoid an underestimation of the multi-prong signal caused by a correlation in the N_{track}^{c+c} distribution with the dominant background contribution. Instead, the relative proportion of 1-prong and multi-prong

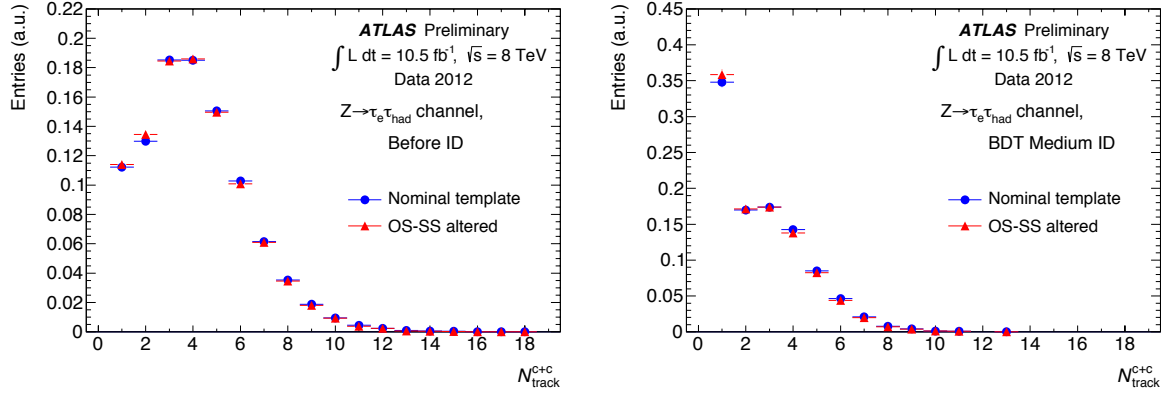


Figure 11: $Z \rightarrow \tau_e \tau_{\text{had}}$ channel: nominal background template from data in same-sign control region and systematically altered background template before tau ID (left) and after BDT medium tau ID (right). The distribution shown is the sum of core and p_T -correlated tracks.

$\tau_{\text{had-vis}}$ is fixed in the fit before identification to the value predicted by simulations. This method relies on the assumption that the reconstruction efficiency is well-modeled in simulated samples for 1-prong and multi-prong $\tau_{\text{had-vis}}$. For the fit after identification, the 1-prong and multi-prong normalizations are still left to vary independently. The dataset used for the measurement amounts to a total integrated luminosity of $L_{\text{int}} = 10.5 \text{ fb}^{-1}$ and $L_{\text{int}} = 8.5 \text{ fb}^{-1}$, for the electron and the muon channel, respectively. The fits for the measurement of the efficiency can be seen in Figures 12 and 13.

The inclusive scale factor results are reported in Tables 3 and 4, while the 1-prong and multi-prong results can be found in Appendix B, Tables 10, 11, 12 and 13. The results in bins of η can be found in Tables 14 and 15.

4.2.5 Combination of $Z \rightarrow \tau_{\text{lep}} \tau_{\text{had}}$ Results

In this section the combination of the scale factor results obtained in the $Z \rightarrow \tau_{\text{lep}} \tau_{\text{had}}$ channels (electron and muon) is discussed. These two channels offer the highest degree of precision, and their combination leads to a further reduction in the total uncertainties. To combine the two measurements, prescriptions are followed according to Ref. [31]. Systematic uncertainties affecting both measurements and coming from the same source are assumed to be fully correlated; otherwise, they are considered to be uncorrelated.

The combination of the inclusive measurements is reported in Table 5. The correlation (ρ) shown in the table corresponds to the total correlation between the measurements and includes the effect of the statistical uncertainties. The results in bins of pseudorapidity can be found in Table 6. The corresponding Figure 14 shows the comparison between the overall and the binned measurement. Tables for the scale factor combination for the exclusive 1-prong (Table 16) and multi-prong (Table 17) results can be found in Appendix B.

4.3 Measurement with $W \rightarrow \tau \nu$ Events

4.3.1 Event Selection

In this section, the measurement of the $\tau_{\text{had-vis}}$ identification efficiency scale factors using $W \rightarrow \tau_{\text{had}} \nu_\tau$ events is presented. The data were recorded in 2012 and correspond to an integrated luminosity of 14.3 fb^{-1} . Events are selected using two triggers: both triggers require the missing transverse energy in the event (E_T^{miss}) to be larger than 80 GeV, with one having a looser E_T^{miss} requirement at an earlier trigger stage. This lower requirement leads to a slightly improved efficiency at low E_T^{miss} values. These

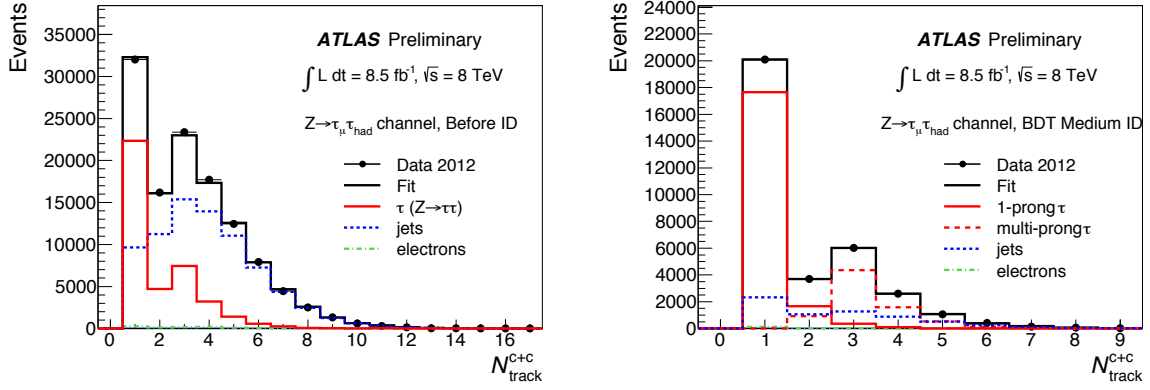


Figure 12: $Z \rightarrow \tau_\mu \tau_{\text{had}}$ channel: fit result before tau ID (left) and after BDT medium tau ID (right) for the measurement of the 1-prong and multi-prong identification efficiencies. All ID methods and working points are included in the same fit. The tau signal template and the electron template are taken from simulations. The jet template is obtained from data in a control region. The distribution shown is the sum of core and p_T -correlated tracks.

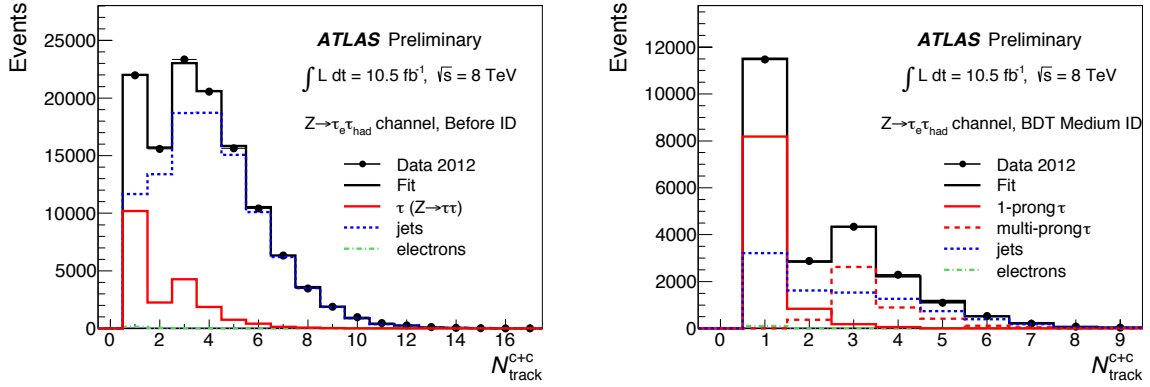


Figure 13: $Z \rightarrow \tau_e \tau_{\text{had}}$ channel: fit result before tau ID (left) and after BDT medium tau ID (right) for the measurement of the 1-prong and multi-prong identification efficiencies. All ID methods and working points are included in the same fit. The tau signal template and the electron template are taken from simulations. The jet template is obtained from data in a control region. The distribution shown is the sum of core and p_T -correlated tracks.

$Z \rightarrow \tau_\mu \tau_{\text{had}}$	Inclusive scale factors and uncertainties					
	BDT			LLH		
	Loose	Medium	Tight	Loose	Medium	Tight
Generator	0.4%	0.2%	0.6%	0.4%	0.3%	0.4%
Hadronic shower	0.4%	0.5%	1.0%	0.5%	0.5%	0.8%
Simulation tune	0.1%	0.1%	0.1%	0.1%	0.2%	0.1%
Detector geometry	0.1%	0.1%	0.2%	0.1%	0.1%	0.4%
Pile-up	0.2%	0.1%	0.1%	0.2%	0.1%	0.1%
OS-SS	2.0%	2.3%	2.4%	2.3%	2.4%	2.4%
Electron	1.5%	0.4%	0.6%	0.6%	0.8%	0.9%
$\Delta\text{SF}^{\text{syst}}$	2.5%	2.4%	2.7%	2.5%	2.6%	2.8%
$\Delta\text{SF}^{\text{stat}}$	1.3%	1.5%	1.9%	1.3%	1.5%	1.9%
$\Delta\text{SF}^{\text{stat+syst}}$	2.9%	2.8%	3.3%	2.8%	3.0%	3.3%
SF	1.001	0.970	0.895	1.001	0.969	0.929

Table 3: $Z \rightarrow \tau_\mu \tau_{\text{had}}$ channel: inclusive scale factors for all ID working points. The systematic uncertainty from each source is also shown.

$Z \rightarrow \tau_e \tau_{\text{had}}$	Inclusive scale factors and uncertainties					
	BDT			LLH		
	Loose	Medium	Tight	Loose	Medium	Tight
Generator	1.1%	1.2%	0.6%	1.1%	1.5%	1.1%
Hadronic shower	0.6%	0.8%	1.6%	0.4%	0.6%	1.4%
Simulation tune	1.2%	1.1%	1.3%	1.2%	1.3%	1.0%
Detector geometry	0.1%	0.1%	0.1%	0.2%	0.2%	0.6%
Pile-up	0.1%	0.1%	0.1%	0.2%	0.1%	0.1%
OS-SS	1.0%	2.8%	4.3%	0.8%	1.1%	2.6%
Electron	0.3%	0.1%	0.1%	0.3%	0.1%	0.3%
$\Delta\text{SF}^{\text{syst}}$	2.0%	3.3%	4.8%	1.8%	2.4%	3.4%
$\Delta\text{SF}^{\text{stat}}$	1.5%	1.7%	2.3%	1.5%	1.7%	2.2%
$\Delta\text{SF}^{\text{stat+syst}}$	2.5%	3.8%	5.3%	2.3%	3.0%	4.1%
SF	1.056	0.996	0.954	1.075	1.002	0.964

Table 4: $Z \rightarrow \tau_e \tau_{\text{had}}$ channel: inclusive scale factors for all ID working points. The systematic uncertainty from each source is also shown.

Combination of inclusive scale factors and uncertainties (%)						
$Z \rightarrow \tau_{\text{lep}} \tau_{\text{had}}$	BDT			LLH		
	Loose	Medium	Tight	Loose	Medium	Tight
SF ($Z \rightarrow \tau_{\mu} \tau_{\text{had}}$)	1.001	0.970	0.895	1.001	0.969	0.929
uncorr syst.	2.0%	2.3%	2.4%	2.3%	2.4%	2.4%
corr syst.	1.6%	0.7%	1.3%	0.9%	1.0%	1.3%
stat.	1.3%	1.5%	1.9%	1.3%	1.5%	1.9%
syst.+stat.	2.9%	2.8%	3.3%	2.8%	3.0%	3.3%
SF ($Z \rightarrow \tau_e \tau_{\text{had}}$)	1.056	0.996	0.954	1.075	1.002	0.964
uncorr syst.	1.0%	2.8%	4.3%	0.8%	1.1%	2.6%
corr syst.	1.7%	1.8%	2.1%	1.7%	2.1%	2.1%
stat.	1.5%	1.7%	2.3%	1.5%	1.7%	2.3%
syst.+stat.	2.5%	3.8%	5.3%	2.3%	3.0%	4.1%
SF Combination	1.033	0.979	0.907	1.044	0.985	0.941
syst.	2.0%	2.1%	2.6%	1.7%	2.1%	2.4%
stat.	1.0%	1.1%	1.5%	1.0%	1.1%	1.5%
syst.+stat.	2.2%	2.4%	3.0%	2.0%	2.4%	2.8%
ρ (total)	0.387	0.121	0.159	0.219	0.242	0.203

Table 5: $Z \rightarrow \tau_{\text{lep}} \tau_{\text{had}}$ combination: inclusive scale factors and uncertainties for all ID working points.

$Z \rightarrow \tau_{\text{lep}} \tau_{\text{had}}$ combination	Inclusive scale factors and \pm syst.unc. \pm stat.unc.		
	Overall	Barrel	End-cap
BDT Loose	$1.033 \pm 2.0\% \pm 1.0\%$	$1.021 \pm 2.1\% \pm 1.2\%$	$1.000 \pm 2.9\% \pm 1.6\%$
BDT Medium	$0.979 \pm 2.1\% \pm 1.1\%$	$0.966 \pm 2.8\% \pm 1.3\%$	$0.954 \pm 2.2\% \pm 1.8\%$
BDT Tight	$0.907 \pm 2.6\% \pm 1.5\%$	$0.941 \pm 3.0\% \pm 1.6\%$	$0.905 \pm 2.4\% \pm 2.2\%$
LLH Loose	$1.044 \pm 1.7\% \pm 1.0\%$	$1.027 \pm 2.4\% \pm 1.2\%$	$1.000 \pm 2.5\% \pm 1.6\%$
LLH Medium	$0.985 \pm 2.1\% \pm 1.1\%$	$0.979 \pm 2.7\% \pm 1.4\%$	$0.927 \pm 3.2\% \pm 1.8\%$
LLH Tight	$0.941 \pm 2.4\% \pm 1.5\%$	$0.925 \pm 3.2\% \pm 1.8\%$	$0.901 \pm 2.8\% \pm 2.3\%$

Table 6: $Z \rightarrow \tau_{\text{lep}} \tau_{\text{had}}$ combination: scale factors for inclusive $\tau_{\text{had-vis}}$ for all ID working points. The measurement binned in $|\eta(\tau_{\text{had-vis}})|$ is compared to the overall results. The barrel region corresponds to $|\eta(\tau_{\text{had-vis}})| < 1.37$, while the end-cap to $|\eta(\tau_{\text{had-vis}})| > 1.52$.

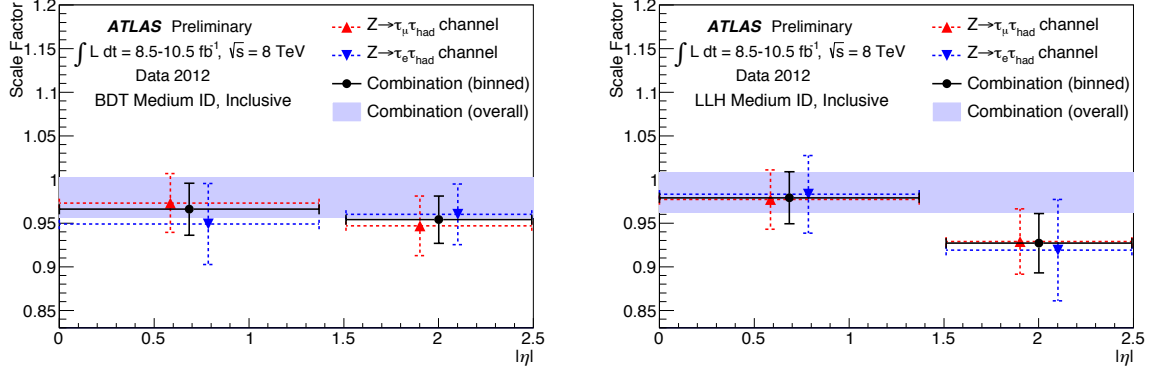


Figure 14: $Z \rightarrow \tau_{\text{lep}}\tau_{\text{had}}$ combination: the combination result of the scale factors between $Z \rightarrow \tau_{\mu}\tau_{\text{had}}$ and $Z \rightarrow \tau_e\tau_{\text{had}}$ channels for the inclusive $\tau_{\text{had-vis}}$ identification efficiency as a function of the pseudorapidity for the working points BDT medium and LLH medium. The full set of working points can be found in Appendix B. The binning corresponds to the barrel and the end-cap regions of the ATLAS detector. The plot includes a comparison to the overall combination result.

are the lowest-threshold unprescaled triggers in the data which can be used in this analysis. Only events recorded with good detector conditions are used, which have a primary vertex with 4 or more associated tracks.

To reduce the contamination from $W \rightarrow \mu\nu_{\mu}$ and $W \rightarrow e\nu_e$ backgrounds, events are required to have no selected light leptons (electron or muon). Muons are required to pass loose identification criteria [32] and to have $p_T > 8 \text{ GeV}$, $|\eta| < 2.5$. To ensure the muons are coming from the collision point, $|z_0|$ is required to be less than 10 mm. Electrons are reconstructed with the calorimeter-based reconstruction and are required to pass a medium identification with cluster $E_T > 15 \text{ GeV}$, and are required to be in the fiducial volume $|\eta| < 1.37$, $1.52 < |\eta| < 2.47$. Any event with an electron or muon fulfilling the above requirements is rejected.

The events are required to have at least one $\tau_{\text{had-vis}}$ candidate with $p_T > 20 \text{ GeV}$ and $|\eta| < 2.47$. To reduce contamination from electrons, the e -veto BDT score for $\tau_{\text{had-vis}}$ candidates is required to be greater than 0.4. To improve the probability of selecting the correct $\tau_{\text{had-vis}}$ candidate before $\tau_{\text{had-vis}}$ identification is applied, the candidates are also required to have transverse mass $m_T < 80 \text{ GeV}$ and $\Delta\phi(\tau_{\text{had-vis}}, E_T^{\text{miss}}) < 2.0$. The transverse mass m_T of the $\tau_{\text{had-vis}}$ candidate and E_T^{miss} is here defined as:

$$m_T = \sqrt{2 \cdot p_T(\tau_{\text{had-vis}}) \cdot E_T^{\text{miss}} \cdot (1 - \cos \phi(\tau_{\text{had-vis}}, E_T^{\text{miss}}))} . \quad (3)$$

If more than one candidate passes the selection, the candidate with m_T closest to 50 GeV is chosen.

To reduce the contamination from $t\bar{t}$ and $b\bar{b}$ events, events are rejected if there are any jets passing the 85% b -jet efficiency working point [33]. This cut is important for the extraction of the jet template from data in a control region described in Section 4.3.2. Events are also required to have fewer than 5 jets. To reject events with fake missing transverse energy coming from poorly reconstructed jets, any event with a jet or $\tau_{\text{had-vis}}$ candidate with $p_T > 20 \text{ GeV}$ within $\Delta\phi < 0.5$ of the E_T^{miss} direction is rejected. Finally, to further improve signal purity, the following requirements are made on the reconstructed missing transverse energy $E_T^{\text{miss}} > 100 \text{ GeV}$ and E_T^{miss} significance $S_{E_T^{\text{miss}}} > 12$. The latter is defined as follows:

$$S_{E_T^{\text{miss}}} = \frac{E_T^{\text{miss}}}{0.5 \sqrt{\sum E_T^{\text{jets}}}} , \quad (4)$$

where ΣE_T^{jets} is the scalar sum of the E_T of all jets in the event. After the selection requirements detailed above are applied, the remaining main backgrounds come from fake jets which are associated with $Z \rightarrow \nu\nu$ events (electroweak + jets events). There is also a small contribution from multi-jet events.

4.3.2 Backgrounds and Templates

The templates for the $\tau_{had-vis}$ signal and the electron background are obtained from samples simulated with ALPGEN and PYTHIA, respectively. The template for $\tau_{had-vis}$ is obtained from simulated $W \rightarrow \tau\nu$ events where the $\tau_{had-vis}$ candidate is matched to a true hadronically decaying tau lepton. The electron template is obtained from simulated $W \rightarrow e\nu$ events where the $\tau_{had-vis}$ candidate is also required to be matched to a true electron from the W . In both cases, the full event selection discussed in Section 4.3.1 is applied.

The template for jets is obtained from a control region which uses the same selection as the signal region, except that a reconstructed muon is now required instead of a $\tau_{had-vis}$. The $\tau_{had-vis}$ candidates from such events are therefore expected to come from fake jets. To ensure the purity of this $W \rightarrow \mu\nu + jets$ sample, the muon selection is tightened. The muons are required to pass the same selection cuts as the muons in Section 4.3.1 with $p_T > 18$ GeV. In addition, the muons are required to have a track in the inner detector and the muon spectrometer ('combined muons'). The muons must fulfill the quality requirements on the track and the isolation requirements, requiring that no additional tracks in the region $\Delta R < 0.4$ are present, and requiring that the sum of the transverse calorimeter energy deposits in the region $0.05 < \Delta R < 0.2$ is less than 4% relative to the muon p_T . Finally, to reduce the contamination from $W \rightarrow \tau\nu$, $Z \rightarrow \tau\tau$ and multi-jets events, muons are required to have transverse mass $m_T(\mu, E_T^{miss}) > 45$ GeV. Any $\tau_{had-vis}$ candidates within $\Delta R = 0.4$ of a selected muon is removed.

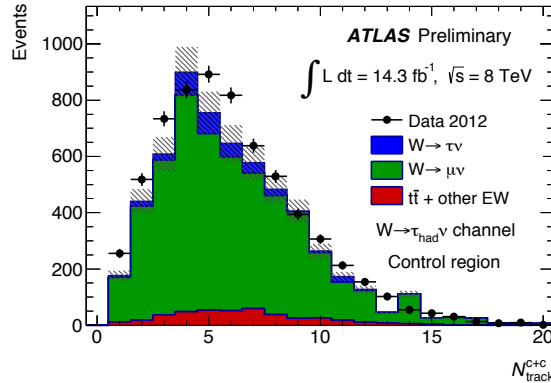


Figure 15: $W \rightarrow \tau_{had-vis}\nu$ channel: extended track multiplicity distribution in the jet control region. The distributions from simulations are normalized to the integrated luminosity.

Figure 15 shows the distribution of the extended track multiplicity associated to $\tau_{had-vis}$ candidates in the jet control region. The region is dominated by $W \rightarrow \mu\nu + jets$ and has a small contamination from $t\bar{t}$ events. If the veto on b -tagged jets is removed, the contamination from $t\bar{t}$ events increases and the jet template has non-negligible contribution from real $\tau_{had-vis}$ from top decays, especially after the tight ID requirement. This effect lowers the separation power between the $\tau_{had-vis}$ and jet templates, and could lead to potential biases. This is the reason why events containing any b -tagged jets are vetoed. Similarly as for the signal region, the fake jets in the control region come dominantly from electroweak + jets events. This ensures that this control region provides a template which appropriately models the jet backgrounds in the signal region.

4.3.3 Systematic Uncertainties

Systematic uncertainties are evaluated by taking the difference between the nominal fitting results and fitting results obtained using alternative templates. Different sources of systematic uncertainties are considered separately for each template.

For the tau signal template, simulation uncertainties are taken into account. In this measurement, the list of uncertainties are the following: choices of event generator, shower modeling, fragmentation model parameters and ambiguity of detector geometry. The difference between the nominal templates and the alternative templates are very small except for differences between the PYTHIA and ALPGEN event generators, and between the different showering models.

In addition, a pile-up uncertainty is evaluated by varying the scale factor used during the pile-up reweighting. The differences between the nominal and alternative templates are very small.

For the electron template, the uncertainty on the normalization after tau ID is considered. Alternative templates are obtained by varying the electron template normalization between the predictions from simulations and the prediction $\pm 1\sigma$ of the e -veto scale factor uncertainty. The normalization of the electron template before tau ID is constrained to the predictions from simulated events.

For the jet template, the uncertainty comes from the different relative fraction of quark- and gluon-initiated jets in the signal and control regions. This systematic uncertainty is estimated by removing the E_T^{miss} significance requirement; by doing so, the contribution from multi-jets events is enhanced. In addition, the uncertainty from the contamination from real $\tau_{\text{had-vis}}$ is considered. This systematic uncertainty is evaluated by enhancing the $t\bar{t}$ events which include real $\tau_{\text{had-vis}}$ from the top decay. Alternative templates are created by loosening the b -jet event veto, using the 60% b -jet efficiency point. Figure 16 shows the nominal and alternative jet templates for the uncertainty due to the quark-gluon fraction and contamination from real $\tau_{\text{had-vis}}$ before ID and after BDT medium tau ID.

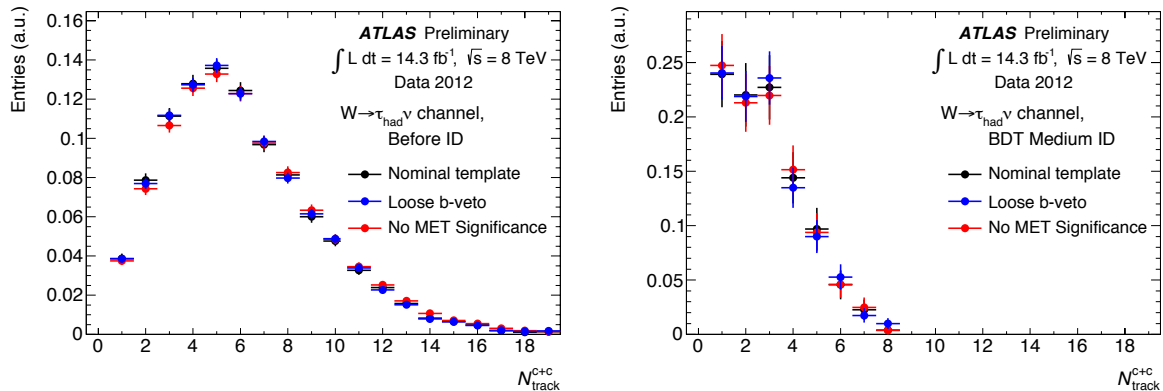


Figure 16: $W \rightarrow \tau_{\text{had}}\nu$ channel: nominal jet template and alternative templates for the uncertainty of quark-gluon fraction and contamination from real $\tau_{\text{had-vis}}$. The plot on the left (right) shows the template before tau ID (after BDT medium tau ID). The distribution shown is the sum of core and p_T -correlated tracks.

4.3.4 Fit and Results

The results of the inclusive extended track multiplicity fitting for $\tau_{\text{had-vis}}$ candidates are shown in Figure 17. The fitting is performed simultaneously for all ID working points. The measured scale factors of tau ID efficiency are summarized in Table 7 for all working points.

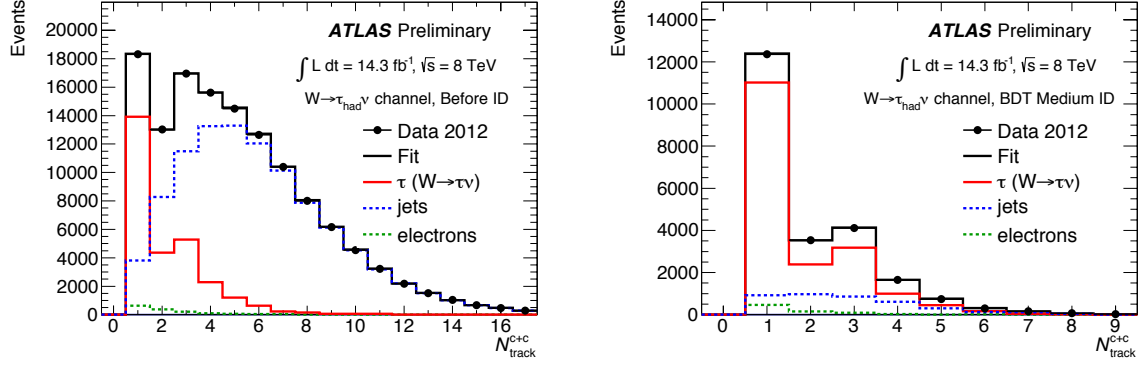


Figure 17: $W \rightarrow \tau_{\text{had}}\nu$ channel: fit result before tau ID (left) and after BDT medium tau ID (right) for the measurement of the inclusive ID efficiency. All ID working points are included in the same fit. The tau signal template and the electron template are obtained from simulation. The jet template is obtained from the data-driven control region. The distribution shown is the sum of core and p_T -correlated tracks.

$W \rightarrow \tau_{\text{had}}\nu$	Inclusive scale factors and uncertainties (%)					
	BDT			LLH		
	Loose	Medium	Tight	Loose	Medium	Tight
Generator	1.2%	0.9%	1.4%	0.6%	0.8%	1.9%
Hadronic shower	1.8%	1.9%	0.9%	1.4%	1.5%	1.7%
Simulation tune	0.2%	0.1%	0.5%	0.4%	0.9%	0.1%
Detector geometry	0.4%	0.7%	0.8%	0.7%	1.3%	1.0%
Pile-up	0.1%	0.1%	0.1%	0.1%	0.1%	0.1%
No MET Sig	2.1%	2.4%	2.4%	2.4%	2.3%	2.8%
Loose b -jet veto	0.2%	0.5%	1.3%	0.7%	1.0%	3.0%
Electron	1.7%	1.4%	3.0%	2.0%	1.8%	2.0%
$\Delta\text{SF}^{\text{syst}}$	3.5%	3.6%	4.5%	3.6%	3.9%	5.3%
$\Delta\text{SF}^{\text{stat}}$	3.1%	3.0%	3.1%	3.4%	3.4%	3.7%
$\Delta\text{SF}^{\text{stat+syst}}$	4.6%	4.7%	5.4%	5.0%	5.2%	6.5%
SF	0.979	0.958	0.942	0.974	0.957	0.887

Table 7: $W \rightarrow \tau_{\text{had}}\nu$ channel: inclusive scale factors for all ID working points. The systematic uncertainty from each source is also shown.

4.4 Measurement with $t\bar{t} \rightarrow \tau + \text{jets}$ Events

In proton-proton collisions at $\sqrt{s} = 8$ TeV, the $t\bar{t}$ production cross section is theoretically predicted to be 238^{+22}_{-24} pb [34]. With the large integrated luminosity provided by the 2012 ATLAS dataset, a sample of hundreds of thousands of top quark pairs can be studied. Roughly 10% of these pairs will decay producing the final state $t\bar{t} \rightarrow [b\tau_{\text{had}}\nu_\tau][bqq]$. The large backgrounds in this channel render the identification of this final state experimentally difficult. However, the high mass of the t -quark allows to study τ_{had} in a high momentum range that cannot be studied in other channels. Furthermore, the large jet multiplicity in the final state gives the possibility of measuring the performance of $\tau_{\text{had-vis}}$ identification algorithms in busier event environments.

4.4.1 Event Selection

Events are selected using either of two triggers: one selects events based on the presence of at least 4 jets, 2 of those being b -tagged, while the other requires 80 GeV of $E_{\text{T}}^{\text{miss}}$. To isolate the desired final state and reject the various backgrounds, the following requirements are made:

- at least 5 jets with $p_{\text{T}} > 20$ GeV and $|\eta| < 2.5$,
- of which at least two are identified as b -jets using the 60% efficiency working point [33],
- no reconstructed electrons or muons with $p_{\text{T}} > 15$ GeV and $|\eta| < 2.5$, to reduce contributions from electroweak processes,
- $S_{E_{\text{T}}^{\text{miss}}} > 8$, as defined in Equation 4 (note that, due to the large jet multiplicity of $t\bar{t}$ events, most events passing this requirement will also pass the 80 GeV $E_{\text{T}}^{\text{miss}}$ requirement of the corresponding trigger),
- no jets coming from a spurious energy deposit in the calorimeters in the events,
- e -veto BDT score > 0.4 for $\tau_{\text{had-vis}}$ candidates with one core track.

These cuts are very stringent compared to the other channels, and lead to a rather low signal efficiency. However, the multi-jet backgrounds in this channel are extremely large (due to the small $t\bar{t}$ cross section, in comparison to the W channel, for example), and such stringent cuts are necessary to obtain a satisfactory level of background rejection. As the jet multiplicity is large, it is necessary to determine a strategy for choosing which $\tau_{\text{had-vis}}$ candidate is to be used for each event (as each jet represents a possible candidate). In the chosen procedure, a combination of three of the jets in the event are hypothesized to correspond to the decay products of the hadronically decaying t -quark, and are rejected from the selection. These three jets are chosen such that, when their 4-vectors are vectorially added, the resulting vector has the largest p_{T} . Exactly one of these three jets is required to be b -tagged. The largest- p_{T} non- b -tagged jet remaining is taken as the $\tau_{\text{had-vis}}$ candidate. This approach identifies the jet associated to the real $\tau_{\text{had-vis}} \sim 50\%$ of the time.

4.4.2 Backgrounds and Templates

The contribution from hadronically decaying tau leptons as well as from electrons mis-identified as $\tau_{\text{had-vis}}$ are taken from simulated $t\bar{t}$ events. Both are combined into a single template, with the relative mixture fixed according to simulations. This ensures a stable fit, as the main difference between both templates occurs in a region of the $N_{\text{track}}^{\text{c+c}}$ distribution where background contributions from mis-identified jets are sizable.

The dominating background contributions come from jets, both from $t\bar{t}$ events (with a large quark-initiated jet contribution) and multi-jet events (dominated by gluon-initiated jets). To estimate the contribution from multi-jet events, a sideband region with a lower $S_{E_T^{\text{miss}}}$ requirement is used ($3 < S_{E_T^{\text{miss}}} < 4$). Such a region has a contribution from $t\bar{t}$ events at the percent level, and therefore gives a pure sample of multi-jet events. The dependence of the N_{track}^{c+c} distribution on the event $S_{E_T^{\text{miss}}}$ is found to be very small, as shown in Figure 18(a), and the differences are taken as a systematic uncertainty. The template obtained from this selection is referred to as the gluon-jet template. To model the mis-identified jets from $t\bar{t}$ events where the wrong jet is picked as $\tau_{\text{had-vis}}$ candidate, a different analysis selection is used to isolate $t\bar{t} \rightarrow \mu + \text{jets}$ events. This selection consists of the default selection, requiring now that a tight muon [32] be reconstructed, and requiring one less jet in the final state. The two leading jets in the event are then taken as the $\tau_{\text{had-vis}}$ candidates. A re-weighting based on the p_T distribution of the candidates is used to account for the different kinematics of the jets in the $\mu + \text{jets}$ sample with respect to the original $\tau + \text{jets}$ sample. Also, a small simulation-based correction must be applied to remove the contribution from di-lepton events with a $\mu + \tau_{\text{had-vis}}$ final state. This template is referred to as the quark-jet template. Figure 18(b) shows the closure test of the method in simulations, comparing the N_{track}^{c+c} of jets in simulated $t\bar{t} \rightarrow \tau + \text{jets}$ events with jets in simulated $t\bar{t} \rightarrow \mu + \text{jets}$. A good agreement is observed, proving that the data-driven method can be used to obtain a background template for the signal region.

While the shapes of these two templates are different enough to have their normalizations determined by the fit, much smaller statistical uncertainties can be obtained by constraining the ratio of the normalization of the $t\bar{t}$ jet fakes to the $t\bar{t}$ $\tau_{\text{had-vis}}$ signal using simulations. A soft constraint is used, allowing the normalizations to float freely within a Gaussian of a width of 20% of the value taken from the simulated events.

In the high- p_T regime where this measurement is performed, applying the identification algorithms introduces a bias in the template shapes. Jet fakes with a large number of associated tracks are strongly suppressed, and only the lowest N_{track}^{c+c} bins in the background templates remain populated. This means that a fit can no longer be used to determine the background normalizations as there is too little information in the N_{track}^{c+c} distribution. Instead of obtaining the number of background events after identification criteria from a fit, it is instead extrapolated from the the number of fitted background events before identification. In order to determine how many of the jet fakes estimated from the fit would pass the identification requirements, the efficiency of the identification algorithms is measured on a sample enriched in these jet fakes. These measured efficiencies are referred to as fake-efficiencies, and are typically much lower than for real $\tau_{\text{had-vis}}$, due to the high rejection power of the identification algorithms. These fake-efficiencies are derived from two samples. To model gluon-like fakes, a multi-jet control sample is obtained by looking at events accepted by a combination of multi-jet triggers, and required to have $E_T^{\text{miss}} < 20 \text{ GeV}$. This gives a highly gluon-enriched sample with a negligible contribution from real $\tau_{\text{had-vis}}$. To model quark-like fakes, a $\gamma + \text{jets}$ sample is used, requiring a tight, isolated photon [35] with $p_T > 40 \text{ GeV}$. Both control samples additionally have an electron and muon veto applied, to reduce contributions from W and Z processes. The fake-efficiencies are derived as a function of $\tau_{\text{had-vis}}$ p_T . To obtain the number of background events after identification, the number of events before identification are multiplied by the relevant fake-efficiencies, taking into account the p_T distribution of the jet fakes. A sample distribution of fake-efficiencies is shown in Figure 19.

4.4.3 Systematic Uncertainties

To estimate the effect of systematic uncertainties on the fit results, a pseudo-experiment approach is used. The fit is repeated many times with the templates being varied according to the different systematic prescriptions.

The systematic uncertainties on the combined $\tau_{\text{had-vis}}$ and electron template come from the possible

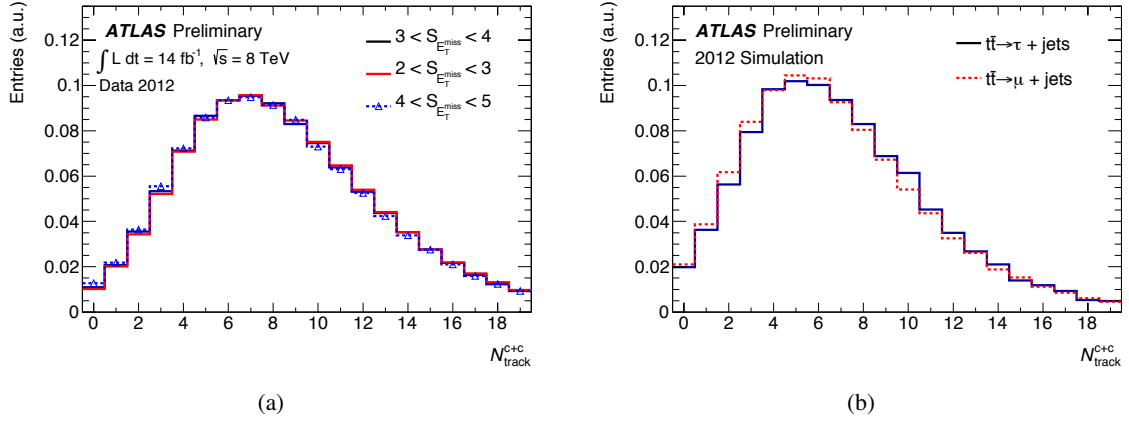


Figure 18: $t\bar{t} \rightarrow \tau + \text{jets}$ channel: extended track multiplicity spectrum of the $\tau_{\text{had-vis}}$ candidates for both background templates. For the gluon-jet template (a), the dependence on the $S_{E_T^{\text{miss}}}$ criteria is shown. For the quark-jet template (b), a comparison of the expected templates from $t\bar{t} \rightarrow \tau + \text{jets}$ and $t\bar{t} \rightarrow \mu + \text{jets}$ events in simulation is shown, to illustrate the closure of the method.

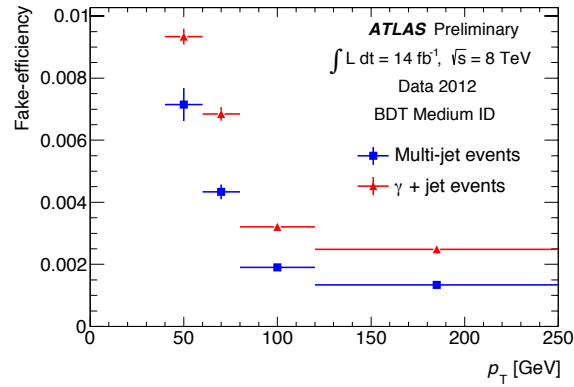


Figure 19: $t\bar{t} \rightarrow \tau + \text{jets}$ channel: fake-efficiencies measured from both control samples for the BDT medium tau identification. Only statistical uncertainties are shown.

mis-modeling by the generator used. Uncertainties are taken on the relative $\tau_{\text{had-vis}}$ and electron normalizations (from studies of the electron veto), and on the amount of ISR/FSR generated in the collision. Other generator and detector modeling uncertainties were found to be negligible.

For the quark-jet template ($\mu + \text{jet}$ sample), uncertainties are taken on the closure of the method in simulations, and to account for the limited statistics of the data-driven control region. An uncertainty of 20% is also taken on the simulation-based subtraction of di-lepton events, based on previous generator studies.

For the gluon-initiated jet template (low $S_{E_T^{\text{miss}}}$ sideband region), uncertainties are taken on the statistics of the sample, and on the dependence on the $S_{E_T^{\text{miss}}}$ criteria used.

For the fake-efficiencies, a conservative uncertainty of 50% is taken on the efficiencies, based on the largest deviation seen between both control samples.

$t\bar{t} \rightarrow \tau + jets$	Inclusive scale factors and uncertainties (%)					
	BDT			LLH		
	Loose	Medium	Tight	Loose	Medium	Tight
$\tau_{\text{had-vis}}$ template						
$\tau_{\text{had-vis}}/e$ ratio	0.3%					
ISR/FSR	1.4%					
Statistical uncertainties	0.8%					
Quark-jet template						
Closure in simulation	1.3%					
Statistical uncertainties (data)	1.6%					
Di-lepton subtraction	0.9%					
Gluon-jet template						
Dependence on $S_{E_{\text{T}}^{\text{miss}}}$ criteria	0.6%					
Statistical uncertainties	0.1%					
Fakes after ID	3.8%	2.2%	1.2%	3.8%	2.4%	1.0%
ΔSF^{syst}	4.8%	3.6%	3.2%	4.8%	3.7%	3.1%
ΔSF^{stat}	4.6%	4.8%	5.5%	4.6%	4.9%	5.6%
$\Delta\text{SF}^{stat+syst}$	7.1%	6.2%	6.5%	7.1%	6.1%	6.5%
SF	1.06	1.04	0.94	1.03	0.98	0.92

Table 8: $t\bar{t} \rightarrow \tau + \text{jets}$ channel: inclusive scale factors for all ID working points. The first part of the table shows the systematic uncertainties associated with each template for the fit before any identification criteria are applied.

4.4.4 Fit and Results

The final fit results before identification are shown in Figure 20. To obtain the number of tau leptons present, the mis-identified electron contribution must be subtracted. This is performed using simulated events, and applying the electron veto scale factors derived in Section 5. The resulting measured scale factors are shown in Table 8, along with the associated uncertainties. Only inclusive results are provided

due to the limited statistics of this sample. These results are applicable to $\tau_{\text{had-vis}}$ candidates with $p_T > 40$ GeV. The dataset used for the measurement amounts to a total integrated luminosity of $L_{\text{int}} = 14 \text{ fb}^{-1}$.

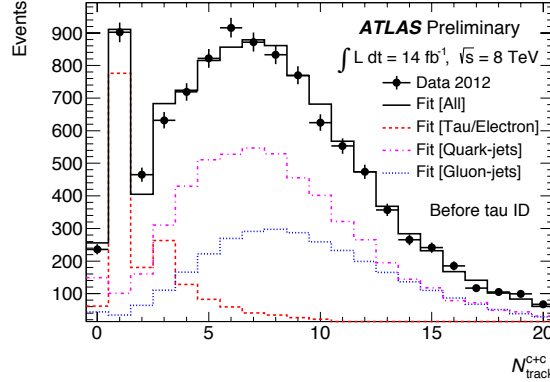


Figure 20: $t\bar{t} \rightarrow \tau + \text{jets}$ channel: Results of the fit before any identification criteria are applied. Only statistical uncertainties are shown. The distribution shown is the sum of core and p_T -correlated tracks.

4.5 Summary

Scale factors for the $\tau_{\text{had-vis}}$ signal efficiency measured in four different final states have been provided. The measurements in all channels agree within uncertainties and no significant tension is found, as demonstrated in Tables 5, 7 and 8. Figure 21 shows a summary of all inclusive measurements and illustrates the good agreement between all channels. The measurements from the $Z \rightarrow \tau_{\text{lep}}\tau_{\text{had}}$ channels (combination of electron and muon channels) have the smallest associated uncertainties (2% to 3% level) and are taken as the main measurement. The $W \rightarrow \tau_{\text{had}}\nu_\tau$ results have associated uncertainties at the 5% to 6% level, and are therefore only used as cross-checks. The scale factors are compatible with unity for the looser working points, and are approximately 10% lower for the tightest efficiency point. This implies that the efficiency is lower in data when more stringent requirements are made on the input variables, and suggests that the input variables and their correlations are not perfectly modeled in simulation.

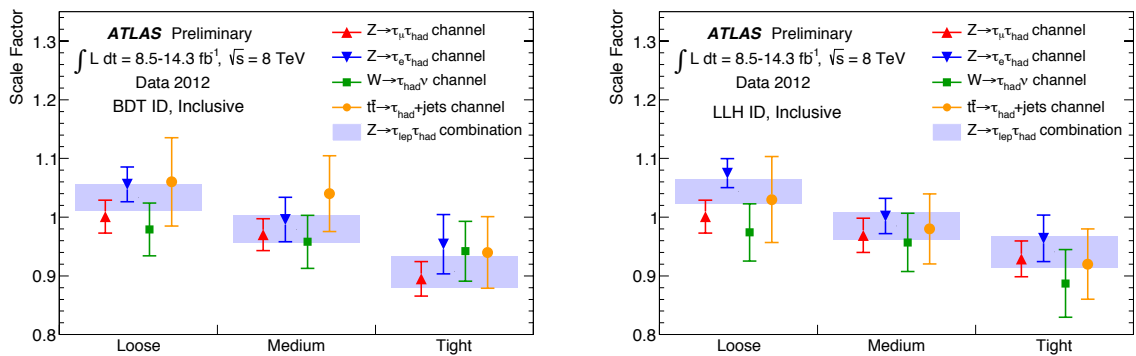


Figure 21: Summary of the inclusive scale factors for all channels and all working points.

For most analyses, the inclusive (overall) scale factors provided in Table 6 are sufficient to correct the $\tau_{\text{had-vis}}$ signal efficiency in simulation. No significant η -dependence has been found in the scale factors,

as demonstrated by the dedicated barrel and end-cap scale factors in Table 6. However, if observables which are highly sensitive to the relative identification efficiency of $\tau_{\text{had-vis}}$ in different detector regions are used in an analysis, the dedicated barrel and end-cap scale factors should be considered. For analyses which treat 1-prong and multi-prong $\tau_{\text{had-vis}}$ candidates separately, or which use observables sensitive to their relative contribution, dedicated scale factors are provided in Tables 16 and 17 in Appendix B. Finally, if a large number of $\tau_{\text{had-vis}}$ candidates used in an analysis are in the high- p_T regime ($p_T > 40$ GeV), the inclusive scale factors from the $t\bar{t} \rightarrow \tau_{\text{had}} + \text{jets}$ measurement should be used for these candidates, as provided in Table 8.

5 Measurement of the Electron Veto Efficiency Scale Factors

As discussed in Section 3.2, the ATLAS electron veto algorithm was tuned using simulated samples to provide specific efficiency working points. It is important to verify that this veto algorithm performs comparably both in simulated samples and in data. This is done by performing direct measurements of the real electron veto efficiency in data for multiple combinations of tau ID, electron veto, and electron overlap removal and comparing it to the efficiency obtained using simulated samples. This measurement is the focus of this section.

The tag-and-probe approach chosen consists of selecting $Z \rightarrow ee$ events with real electrons in their final state, and extracting the efficiencies directly from the number of reconstructed $\tau_{\text{had-vis}}$ before and after identification and/or veto algorithms are applied.

5.1 Event Selection

Events must contain at least one tag object and at least one probe object. Then, all combinations of tag objects and probe objects are considered for the measurement.

The tag object (‘tag electron’) is a reconstructed electron candidate with transverse momentum $p_T(e) > 35$ GeV and pseudorapidity $\eta(e)$ within the fiducial volume defined by the barrel or end-cap detector regions ($|\eta| < 1.37$ or $1.52 < |\eta| < 2.47$). The tag electron is then required to pass a tight electron identification [36]. Two isolation requirements are additionally required of the tag electron to suppress contamination from multi-jet events: the calorimeter energy in a cone of radius $\Delta R < 0.2$ around the tag electron is required to be less than 5% of $p_T(e)$, and the sum of momenta from additional tracks present in a cone of radius $\Delta R < 0.4$ around the tag electron is required to be less than 4% of $p_T(e)$.

The probe object (‘probe tau’) is a reconstructed tau candidate with $p_T(\tau_{\text{had-vis}}) > 20$ GeV and pseudorapidity $\eta(\tau_{\text{had-vis}})$ within the fiducial volume defined by the tracking system ($|\eta(\tau_{\text{had-vis}})| < 2.5$). The probe tau is required to have exactly one track in the core cone, and it is not considered if it overlaps with an identified electron candidate with $\Delta R < 0.2$, where different levels of offline electron identification are considered for the measurement. Additionally, the probe tau is required to have a e -veto BDT score less than 0.75. This requirement strongly suppresses contamination from real $\tau_{\text{had-vis}}$, quark-, and gluon-initiated jets.

After requiring at least one tag electron and probe tau, the event is required to pass either of the two lowest unscaled electron triggers. One of the triggers selects events with an isolated electron with $E_T > 24$ GeV. The other trigger requires the electron to have at least 60 GeV, but puts less constraints on the electron isolation. Then, for each tag-probe combination, the invariant mass of the tag-probe system is required to be within a Z -mass window ($80 \text{ GeV} < m_{\text{vis}}(e, \tau_{\text{had-vis}}) < 100 \text{ GeV}$), and the tag electron and probe tau are required to have opposite charge. No identified muons are allowed in the event. The transverse mass m_T of the tag electron and E_T^{miss} (defined as in Equation 3) is further required to be less than 40 GeV to suppress contamination from $W \rightarrow e\nu$ events.

5.2 Backgrounds

Before applying the electron veto, the $Z \rightarrow ee$ selection is very pure, as shown in Figure 22 (left). After applying the electron veto, the selection is contaminated predominantly by $W \rightarrow e\nu$ events, as well as multi-jet events, $Z \rightarrow \tau\tau$ events, and $t\bar{t}$ events, as shown in Figure 22 (right).

To estimate the multi-jet contamination, the ratio of multi-jet events with same-sign tag electron and probe tau versus opposite-sign is assumed to be unity. The multi-jet contamination is then taken from the $Z \rightarrow ee$ selection in data, but requiring same-sign tag electron and probe tau instead of opposite-sign, and with expected contamination from other processes with same-sign taken from simulations and subtracted.

To estimate the $W \rightarrow e\nu$, $Z \rightarrow \tau\tau$, and $t\bar{t}$ backgrounds, event yields are observed in dedicated control regions for each background, for data and for the prediction from simulations. The difference in event yields is taken as a data-driven normalization for each background. These normalizations are derived for each combination of tau ID, electron veto, and electron overlap removal considered for the measurement. The order of extrapolation is: first, the normalization of $W \rightarrow e\nu$ events is derived; then, the multi-jet estimate is derived; then, the normalization for $t\bar{t}$ events is derived; and last, the normalization for $Z \rightarrow \tau\tau$ events is derived.

5.3 Systematic Uncertainties

Four variations are considered as systematic uncertainties for the measurement. These are varying the tag electron transverse momentum threshold (from 35 GeV to 40 GeV), varying the tag electron calorimeter isolation requirement (from 5% of the momentum to 8%), varying the data-driven normalization of the simulated backgrounds (increased by 1σ of the statistical uncertainty of the normalization) and varying the e -veto BDT score requirement on the probe tau (from 0.75 to 0.85). For all variations, the systematic uncertainty is taken as the difference between the nominal measurement and the varied measurement, and this uncertainty is taken to be symmetric with regard to the nominal measurement.

5.4 Results

The electron veto efficiency for real electrons was compared in data and simulated events with an integrated luminosity of $L_{\text{int}} = 5.8 \text{ fb}^{-1}$. This was measured for 111 combinations of tau ID, electron veto, and electron overlap removal: seven levels of tau ID, four levels of electron veto, and four levels of electron overlap removal, where the disagreement between data and prediction is factored out when no identification or veto algorithms are applied. Within these selections, the efficiency was measured in six regions of $|\eta(\tau_{\text{had-vis}})|$. Four of these regions correspond to the regions used for training the electron veto, and the remaining regions correspond to a gap in the coverage of the Transition Radiation Tracker ($|\eta(e)| < 0.05$) and the end of the coverage of the offline electron identification ($|\eta(e)| > 2.47$).

For brevity, scale factors and the associated uncertainties on the electron efficiency after the veto is applied for only a single combination of tau ID, electron veto, and electron overlap removal are shown in Table 9. The scale factors should only be applied to real electrons in simulated events.

The difference in the efficiency between data and simulation is largest for $|\eta(\tau_{\text{had-vis}})| > 2.0$, as illustrated in Figure 22 (right). This is because the energy deposited in the hadronic calorimeter is not modeled well in the simulations. This energy is part of the electromagnetic fraction (f_{EM}) of the probe tau, and the electron veto relies heavily on f_{EM} for $|\eta(\tau_{\text{had-vis}})| > 2.0$.

Electron veto scale factors and uncertainties						
medium BDT tau ID, medium e -veto, loose electron overlap removal						
$ \eta(\tau_{\text{had-vis}}) $	0.00 – 0.05	0.05 – 1.37	1.37 – 2.00	2.00 – 2.30	2.30 – 2.47	2.47+
vary tag electron p_T	12%	4.5%	7.9%	17%	7.0%	57%
vary tag electron isolation	2.3%	6.3%	2.1%	11%	39%	28%
vary background norm.	1.2%	5.3%	5.7%	1.3%	1.1%	0.1%
vary probe tau e -veto BDT	2.3%	11%	6.4%	16%	8.1%	2.9%
$\Delta\text{SF}^{\text{syst}}$	12%	14%	12%	26%	41%	64%
$\Delta\text{SF}^{\text{stat}}$	13%	12%	19%	13%	19%	17%
$\Delta\text{SF}^{\text{stat+syst}}$	17%	18%	22%	29%	44%	66%
SF	0.86	1.12	1.40	1.58	2.70	21.69

Table 9: Scale factors and the associated systematic uncertainties after applying a medium electron veto, medium BDT tau ID, and after performing overlap removal with reconstructed electron candidates which pass a loose identification [36].

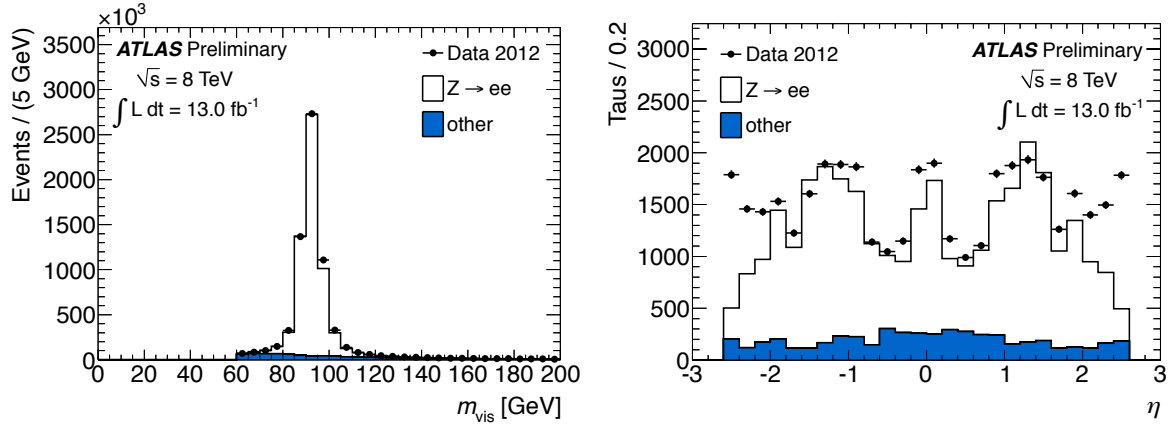


Figure 22: Invariant mass of the tag-probe system $m_{\text{vis}}(e, \tau_{\text{had-vis}})$ before applying any identification, veto algorithms, and/or additional selections to increase the purity of $Z \rightarrow ee$ events (left), and leading track pseudorapidity $\eta(\tau_{\text{had-vis}})$ of the probe tau after applying loose BDT tau ID, loose electron veto, overlap removal with reconstructed electron candidates which pass a tight identification, and additional selections to increase the purity of $Z \rightarrow ee$ events (right). The backgrounds grouped in the ‘other’ category correspond to $W \rightarrow e\nu$, $Z \rightarrow \tau\tau$, $t\bar{t}$ and multi-jet events.

6 Conclusion

The updated reconstruction and identification algorithms for hadronically decaying tau leptons for the 2012 data period have been described in this document. The variables used in the discriminants have been re-optimized to be robust with the increased amount of pile-up present in the 2012 data. The resulting performance of the identification algorithms shows efficiencies which are independent of the number of simultaneous interactions (pile-up). Both supported identification algorithms, BDT tau ID and LLH tau ID, were trained on simulated event samples and data, and provide comparable background rejection and signal efficiency for three pre-determined working points. These algorithms provide rejection factors against multi-jet backgrounds of the order of 60 to 500 for a signal efficiency of 35%. Prescriptions were also provided for rejecting electrons or muons being mis-identified as $\tau_{\text{had-vis}}$ candidates. The cut-based muon-veto was specifically designed to deal with muons which were not properly reconstructed due to poor instrumentation in specific detector regions. The electron-veto uses a multi-variate discriminant, and was optimized using simulated events, providing three fixed efficiency working points. Rejection factors above 100 against background electrons are attained with the tight working point. Finally, the performance of the various identification algorithms was tested in data-driven studies. Measurements of the tau identification algorithm efficiencies were performed using the $Z \rightarrow \tau_{\text{lep}}\tau_{\text{had}}$, $W \rightarrow \tau_{\text{had}}\nu_{\tau}$, and $t\bar{t} \rightarrow \tau_{\text{had}} + \text{jets}$ channels with the goal of providing data to simulation scale factors. The resulting inclusive measurements of the scale factors have relative uncertainties at the 2–3% level. In general, good agreement was found between the performance of the identification algorithms in both simulated events and in data, with slight divergences appearing at the tighter efficiency working points, where the performance is slightly worse in data. Similarly, scale factors were obtained by comparing the efficiency of the electron veto algorithm in data and simulated $Z \rightarrow ee$ events. The performance in the central/barrel region of the detector is found to be well-modeled in simulation. In the region $|\eta| > 2.0$, the calorimeter energy deposits are known to be poorly simulated and a clear discrepancy is observed. Scale factors and associated uncertainties, to be used in correcting simulated samples, are provided for both the identification algorithms and the electron veto.

References

- [1] J. Beringer et al. (Particle Data Group), Phys. Rev. **D86**, 010001 (2012) , <http://pdg.lbl.gov>.
- [2] ATLAS Collaboration, *Measurement of the W to $\tau\nu$ Cross Section in pp Collisions at $\sqrt{s} = 7$ TeV with the ATLAS experiment*, Phys. Lett. **B706** (2012) 276–294, [arXiv:1108.4101](https://arxiv.org/abs/1108.4101) [hep-ex].
- [3] ATLAS Collaboration, *Measurement of the Z to tau tau Cross Section with the ATLAS Detector*, Phys. Rev. **D84** (2011) 112006, [arXiv:1108.2016](https://arxiv.org/abs/1108.2016) [hep-ex].
- [4] ATLAS Collaboration, *Measurement of the top quark pair cross section with ATLAS in pp collisions at $\sqrt{s} = 7$ TeV using final states with an electron or a muon and a hadronically decaying τ lepton*, Phys. Lett. **B717** (2012) 89–108, [arXiv:1205.2067](https://arxiv.org/abs/1205.2067) [hep-ex].
- [5] ATLAS Collaboration, *Measurement of τ polarization in $W \rightarrow \tau\nu$ decays with the ATLAS detector in pp collisions at $\sqrt{s} = 7$ TeV*, Eur. Phys. J. **C72** (2012) 2062, [arXiv:1204.6720](https://arxiv.org/abs/1204.6720) [hep-ex].
- [6] ATLAS Collaboration, *Search for the Standard Model Higgs boson in $H \rightarrow \tau^+\tau^-$ decays in proton-proton collisions with the ATLAS detector*, ATLAS-CONF-2012-160, <http://cds.cern.ch/record/1493624>.
- [7] ATLAS Collaboration, *Search for Neutral MSSM Higgs bosons in $\sqrt{s} = 7$ TeV pp collisions at ATLAS*, ATLAS-CONF-2012-094, <http://cds.cern.ch/record/1460440>.
- [8] ATLAS Collaboration, *Search for charged Higgs bosons decaying via $H^\pm \rightarrow \tau\nu$ in top quark pair events using pp collision data at $\sqrt{s} = 7$ TeV with the ATLAS detector*, JHEP **1206** (2012) 039, [arXiv:1204.2760](https://arxiv.org/abs/1204.2760) [hep-ex].
- [9] ATLAS Collaboration, *A search for high-mass resonances decaying to $\tau^+\tau^-$ in pp collisions at $\sqrt{s} = 7$ TeV with the ATLAS detector*, Phys. Lett. **B719** (2013) 242–260, [arXiv:1210.6604](https://arxiv.org/abs/1210.6604) [hep-ex].
- [10] ATLAS Collaboration, *Search for Supersymmetry in Events with Large Missing Transverse Momentum, Jets, and at Least One Tau Lepton in 7 TeV Proton-Proton Collision Data with the ATLAS Detector*, Eur. Phys. J. **C72** (2012) 2215, [arXiv:1210.1314](https://arxiv.org/abs/1210.1314) [hep-ex].
- [11] ATLAS Collaboration, *Search for third generation scalar leptoquarks in pp collisions at $\sqrt{s} = 7$ TeV with the ATLAS detector*, JHEP **1306** (2013) 033, [arXiv:1303.0526](https://arxiv.org/abs/1303.0526) [hep-ex].
- [12] ATLAS Collaboration, *The ATLAS Experiment at the CERN Large Hadron Collider*, JINST **3** (2008) S08003.
- [13] L. Evans and P. Bryant, *LHC Machine*, JINST **3** (2008) S08001.
- [14] T. Sjostrand, S. Mrenna, and P. Z. Skands, *A Brief Introduction to PYTHIA 8.1*, Comput. Phys. Commun. **178** (2008) 852–867, [arXiv:0710.3820](https://arxiv.org/abs/0710.3820) [hep-ph].
- [15] M. L. Mangano, M. Moretti, F. Piccinini, R. Pittau, and A. D. Polosa, *ALPGEN, a generator for hard multiparton processes in hadronic collisions*, JHEP **07** (2003) 001, [arXiv:hep-ph/0206293](https://arxiv.org/abs/hep-ph/0206293).
- [16] S. Agostinelli et al., *GEANT4: A simulation toolkit*, Nucl. Instr. and Meth. **A506** (2003) 250.
- [17] G. Folger and J. P. Wellisch, *String parton models in Geant4*, [arXiv:nuc1-th/0306007](https://arxiv.org/abs/nuc1-th/0306007).

- [18] M. Blann, B. L. Berman, and T. T. Komoto, *Precompound-model analysis of photonuclear reactions*, Phys. Rev. **C28** (1983) no. 6, 2286–2298.
- [19] H. W. Bertini, *Intranuclear-Cascade Calculation of the Secondary Nucleon Spectra from Nucleon-Nucleus Interactions in the Energy Range 340 to 2900 MeV and Comparisons with Experiment*, Phys. Rev. **188** (1969) 1711–1730.
- [20] B. Andersson, G. Gustafson, and B. Nilsson-Almqvist, *A model for low- p_T hadronic reactions with generalizations to hadron-nucleus and nucleus-nucleus collisions*, Nucl. Phys. **B281** (1987) no. 1-2, 289 – 309.
- [21] M. Cacciari, G. P. Salam, and G. Soyez, *The anti- k_t jet clustering algorithm*, JHEP **04** (2008) 063, arXiv:0802.1189 [hep-ph].
- [22] W. Lampl et al., *Calorimeter Clustering Algorithms: Description and Performance*, ATL-LARG-PUB-2008-002, <http://cds.cern.ch/record/1099735>.
- [23] T. Barillari et al., *Local Hadronic Calibration*, ATL-LARG-PUB-2009-001-2, <http://cds.cern.ch/record/1112035>.
- [24] ATLAS Collaboration, *Performance of the ATLAS Inner Detector Track and Vertex Reconstruction in the High Pile-Up LHC Environment*, ATLAS-CONF-2012-042, <http://cds.cern.ch/record/1435196>.
- [25] ATLAS Collaboration, *Performance of the Reconstruction and Identification of Hadronic τ Decays in ATLAS with 2011 Data*, ATLAS-CONF-2012-142, <http://cds.cern.ch/record/1485531>.
- [26] ATLAS Collaboration, *Jet energy scale and its systematic uncertainty for jets produced in proton-proton collisions at $\sqrt{s}=7$ TeV and measured with the ATLAS detector*, ATLAS-CONF-2010-056, <http://cds.cern.ch/record/1281329>.
- [27] ATLAS Collaboration, *Determination of the tau energy scale and the associated systematic uncertainty in proton-proton collisions at $\sqrt{s} = 8$ TeV with the ATLAS detector at the LHC in 2012*, ATLAS-CONF-2013-044, <http://cds.cern.ch/record/1544036>.
- [28] ATLAS Collaboration, *Reconstruction, Energy Calibration, and Identification of Hadronically Decaying Tau Leptons*, ATLAS-CONF-2011-077, <http://cds.cern.ch/record/1353226>.
- [29] TMVA - Toolkit for Multivariate Data Analysis, <http://tmva.sourceforge.net/>, 2011.
- [30] ATLAS Collaboration, *Performance of the Reconstruction and Identification of Hadronic Tau Decays with ATLAS*, ATLAS-CONF-2011-152, <http://cds.cern.ch/record/1398195>.
- [31] M. G. Cox, C. Ei , G. Mana, and F. Pennecchi, *The generalized weighted mean of correlated quantities*, Metrologia **43** (2006) no. 4, S268.
- [32] ATLAS Collaboration, *A measurement of the muon reconstruction efficiency in 2010 ATLAS data using J/ψ decays*, ATLAS-CONF-2012-125, <http://cds.cern.ch/record/1474642>.
- [33] ATLAS Collaboration, *Measurement of the b -tag Efficiency in a Sample of Jets Containing Muons with 5 fb^{-1} of Data from the ATLAS Detector*, ATLAS-CONF-2012-043, <http://cds.cern.ch/record/1435197>.
- [34] M. Beneke, M. Czakon, P. Falgari, A. Mitov, and C. Schwinn, *Threshold expansion of the $gg(q\bar{q}) \rightarrow Q\bar{Q} + X$ cross section at $O(\alpha_s^4)$* , Phys. Lett. **B690** (2010) 483–490.

- [35] ATLAS Collaboration, *Measurements of the photon identification efficiency with the ATLAS detector using 4.9 fb^{-1} of pp collision data collected in 2011*, ATLAS-CONF-2012-123, <http://cds.cern.ch/record/1473426>.
- [36] ATLAS Collaboration, *Electron performance measurements with the ATLAS detector using the 2010 LHC proton-proton collision data*, Eur. Phys. J. **C72** (2012) 1909, arXiv:1110.3174 [hep-ex].
- [37] ATLAS TRT Collaboration, *The ATLAS Transition Radiation Tracker (TRT) proportional drift tube: design and performance*, JINST **3** (2008) P02013, <http://cds.cern.ch/record/1094549>.

Appendices

A Discriminating Variables

The discriminating variables used to separate hadronically decaying tau leptons from jets, electrons and muons are defined as follows:

Core energy fraction (f_{core}): Fraction of transverse energy in the central region ($\Delta R < 0.1$) of the $\tau_{\text{had-vis}}$ candidate:

$$f_{\text{core}} = \frac{\sum_{i \in \{\text{all}\}}^{\Delta R_i < 0.1} E_{T,i}^{\text{EM}}}{\sum_{j \in \{\text{all}\}}^{\Delta R_j < 0.2} E_{T,j}^{\text{EM}}},$$

where $E_{T,i}$ ($E_{T,j}$) is the transverse energy, calibrated at the EM energy scale, deposited in cell i (j), and i runs over the cells in all layers associated with the $\tau_{\text{had-vis}}$ candidate within $\Delta R < 0.1$ of the intermediate axis, while j runs over all cells in all layers within $\Delta R < 0.2$.

Pile-up-corrected core energy fraction ($f_{\text{core}}^{\text{corr}}$): Pile-up-corrected fraction of transverse energy in the central region ($\Delta R < 0.1$) of the $\tau_{\text{had-vis}}$ candidate:

$$\begin{aligned} f_{\text{core}}^{\text{corr}} &= f_{\text{core}} + 0.003 * N_{\text{vtx}} && \text{for } p_T < 80 \text{ GeV} \\ f_{\text{core}}^{\text{corr}} &= f_{\text{core}} && \text{else} \end{aligned}$$

where N_{vtx} is the number of good vertices in the event, defined as the number of pile-up vertices with at least 2 tracks plus the primary vertex, which is required to have at least 4 tracks. p_T is the momentum of the $\tau_{\text{had-vis}}$ candidate, calibrated at the tau energy scale [27].

Leading track momentum fraction (f_{track}):

$$f_{\text{track}} = \frac{p_T^{\text{leadtrk}}}{\sum_{j \in \{\text{all}\}}^{\Delta R_j < 0.2} E_{T,j}^{\text{EM}}},$$

where p_T^{leadtrk} is the transverse momentum of the leading p_T core track of the $\tau_{\text{had-vis}}$ candidate. $E_{T,j}$ is the transverse energy, calibrated at the EM energy scale, deposited in cell j , and j runs over all cells of the calorimeter (EM + Had) in $\Delta R < 0.2$ around the $\tau_{\text{had-vis}}$ intermediate axis.

Note that for candidates with one track, f_{track} is the fraction of the candidate's momentum attributed to the track, compared to the total momentum of the candidate, which can have contributions from the calorimeter deposits from π^0 s and other neutrals.

Pile-up-corrected leading track momentum fraction ($f_{\text{track}}^{\text{corr}}$):

$$f_{\text{track}}^{\text{corr}} = f_{\text{track}} + 0.003 * N_{\text{vtx}}$$

where N_{vtx} is the number of good vertices in the event, defined as the number of pile-up vertices with at least 2 tracks plus the primary vertex, which is required to have at least 4 tracks.

Track radius (R_{track}): p_T -weighted track width:

$$R_{\text{track}} = \frac{\sum_i^{\Delta R_i \leq 0.4} p_{T,i} \Delta R_i}{\sum_i^{\Delta R_i \leq 0.4} p_{T,i}},$$

where i runs over all core and isolation tracks of the $\tau_{\text{had-vis}}$ candidate, within $\Delta R_i \leq 0.4$. ΔR_i is defined relative to the $\tau_{\text{had-vis}}$ intermediate axis and $p_{T,i}$ is the track transverse momentum.

Note that for candidates with only one track total in the core cone and isolation annulus, R_{track} simplifies to the ΔR between the track and the intermediate axis.

Maximum ΔR (ΔR_{max}): The maximal ΔR between a track associated to the $\tau_{\text{had-vis}}$ candidate and the intermediate axis. Only core tracks are considered.

Transverse flight path significance (S_T^{flight}): The decay length significance of the secondary vertex for multi-track $\tau_{\text{had-vis}}$ candidates in the transverse plane:

$$S_T^{\text{flight}} = \frac{L_T^{\text{flight}}}{\delta L_T^{\text{flight}}},$$

where L_T^{flight} is the reconstructed signed decay length, and $\delta L_T^{\text{flight}}$ is its estimated uncertainty. Only core tracks are used for the secondary vertex fit.

Electromagnetic fraction (f_{EM}): Fraction of transverse energy of the $\tau_{\text{had-vis}}$ candidate deposited in the EM calorimeter:

$$f_{\text{EM}} = \frac{\sum_{i \in \{\text{EM } 0-2\}}^{\Delta R_i < 0.2} E_{T,i}^{\text{EM}}}{\sum_{j \in \{\text{all}\}}^{\Delta R_j < 0.2} E_{T,j}^{\text{EM}}},$$

where $E_{T,i}$ ($E_{T,j}$) is the transverse energy, calibrated at the EM energy scale, deposited in cell i (j), and i runs over the cells in the first three layers of the EM calorimeter, while j runs over the cells in all layers of the calorimeter. ΔR_i is defined relative to the $\tau_{\text{had-vis}}$ intermediate axis

Hadronic radius (R_{Had}): Transverse energy weighted shower width in the hadronic (Had) calorimeter

$$R_{\text{Had}} = \frac{\sum_{i \in \{\text{Had}\}}^{\Delta R_i < 0.2} E_{T,i}^{\text{EM}} \Delta R_i}{\sum_{i \in \{\text{Had}\}}^{\Delta R_i < 0.2} E_{T,i}^{\text{EM}}},$$

where $E_{T,i}$ is the transverse energy, calibrated at the EM energy scale, deposited in cell i and i runs over cells in the hadronic calorimeter and also layer 3 of the EM calorimeter within $\Delta R_i \leq 0.2$. ΔR_i is defined relative to the $\tau_{\text{had-vis}}$ intermediate axis.

Track mass (m_{tracks}): Invariant mass of the track system, where the tracks used for the invariant mass calculation use both core and isolation tracks.

TRT HT fraction (f_{HT}): The ratio of high-threshold to low-threshold hits (including outlier hits), in the Transition Radiation Tracker (TRT), for the leading p_T core track. Since electrons are lighter than pions, and therefore have higher Lorentz γ factors, they are more likely to produce the transition radiation that causes high threshold hits in the TRT [37]. This variable can be used to discriminate hadronic 1-prong $\tau_{\text{had-vis}}$ candidates from electrons.

Ring isolation (f_{iso}):

$$f_{\text{iso}} = \frac{\sum_{i \in \{\text{all}\}}^{0.1 < \Delta R < 0.2} E_{T,i}^{\text{EM}}}{\sum_{j \in \{\text{all}\}}^{\Delta R < 0.2} E_{T,j}^{\text{EM}}}.$$

where $E_{T,i}$ ($E_{T,j}$) is the transverse energy, calibrated at the EM energy scale, deposited in cell i (j), and i runs over calorimeter cells in all layers in the associated topocluster of the $\tau_{\text{had-vis}}$ candidate in an annulus within $0.1 < \Delta R < 0.2$ around the intermediate axis, while j runs over cells in a cone of $\Delta R < 0.2$.

Leading track IP significance ($S_{\text{lead track}}$): impact parameter significance of the leading track of the $\tau_{\text{had-vis}}$ candidate in the core region.

$$S_{\text{lead track}} = \frac{d_0}{\delta d_0},$$

where d_0 is the distance of closest approach of the track to the tau vertex the transverse plane, and δd_0 is its estimated uncertainty.

Number of tracks in isolation annulus ($N_{\text{track}}^{\text{iso}}$): Number of tracks reconstructed within $0.2 < \Delta R \leq 0.4$ around the intermediate axis.

Ratio between energy in the EM calorimeter and leading track momentum ($f_{\text{ECAL}}^{\text{leadtrk}}$):

$$f_{\text{ECAL}}^{\text{leadtrk}} = \frac{\sum_{l=0}^{N_{\text{cell}}} E_{\text{T}}^l}{p_{\text{T}}^{\text{leadtrk}}}.$$

where l runs over calorimeter cells associated to $\tau_{\text{had-vis}}$ candidate. Only cells from the presampler and first three layers of the barrel are taken into account. The energy is calculated in the following window ($\Delta\eta \times \Delta\phi$) around the extrapolation of the leading track to the calorimeter surface: 0.075×0.3 in presampler, 0.0475×0.3 , 0.075×0.075 , 1.5×0.075 for the first, second and third layer. $p_{\text{T}}^{\text{leadtrk}}$ denotes the transverse momentum of the leading track associated to $\tau_{\text{had-vis}}$ candidate in the core region.

Ratio between energy in the hadronic calorimeter and leading track momentum ($f_{\text{HCAL}}^{\text{leadtrk}}$):

$$f_{\text{HCAL}}^{\text{leadtrk}} = \frac{\sum_{l=0}^{N_{\text{cell}}} E_{\text{T}}^l}{p_{\text{T}}^{\text{leadtrk}}}.$$

where l runs over calorimeter cells associated to $\tau_{\text{had-vis}}$ candidate. The energy deposit in the first layer of the hadronic calorimeter in a window $\Delta\phi \leq 0.2$ and $\Delta\eta \leq 0.2$ around the extrapolation of the leading track to the calorimeter surface is summed up. To compensate for the missing of the first layer of the hadronic calorimeter in the transition region of the barrel, the energy of the full hadronic calorimeter depth is collected in the region $0.8 \leq |\eta| < 1.2$. $p_{\text{T}}^{\text{leadtrk}}$ denotes the transverse momentum of the leading track associated to $\tau_{\text{had-vis}}$ candidate in the core region.

Secondary energy deposits in the strip compartment ($E_{\text{T,max}}^{\text{strip}}$): The energy in the strip layer of the EM calorimeter is summed over three cells in ϕ and local maxima are searched for in 101 cell sums in η centered around the impact point of the leading track associated to the tau candidate. The energy associated to the leading track is excluded. The variable is only calculated for $|\eta^{\text{leadtrk}}| \leq 1.7$ where the TRT provides discrimination power between electrons and hadrons.

Presampler strip energy fraction (f_{PS}):

$$f_{\text{PS}} = \frac{\sum_{l=0}^{N_{\text{clus}}} E_l^{\text{PS}}}{\sum_{l=0}^{N_{\text{clus}}} E_l}.$$

where l runs over calorimeter clusters associated to the $\tau_{\text{had-vis}}$ candidate, E_l^{PS} denotes the part of cluster energy, calibrated at the LC scale, deposited in the presampler layer of the calorimeter and E_l is the total energy of a calorimeter cluster.

Electromagnetic energy of charged pions over calorimetric electromagnetic energy ($f_{\text{EM}}^{\pi^\pm}$):

$$f_{\text{EM}}^{\pi^\pm} = \frac{\sum_i^{\Delta R \leq 0.2} p_i^{\text{trk}} - \sum_{l=0}^{N_{\text{clus}}} E_l^{\text{Had}}}{\sum_{l=0}^{N_{\text{clus}}} E_l^{\text{EM}}}.$$

where l runs over calorimeter clusters associated to $\tau_{\text{had-vis}}$ candidate, E_l^{Had} denotes the part of cluster energy deposited in the hadronic part of each cluster (including the third layer of the EM calorimeter), E_l^{EM} is the part of cluster energy deposited in the electromagnetic part of each cluster (presampler and first two layers) and i runs over tracks associated to the $\tau_{\text{had-vis}}$ candidate in the core region. All clusters are calibrated at the LC energy scale.

B Supporting Tables

$Z \rightarrow \tau_\mu \tau_{\text{had}}$	1-prong scale factors and uncertainties					
	BDT			LLH		
	Loose	Medium	Tight	Loose	Medium	Tight
Generator	0.5%	0.5%	1.7%	0.3%	0.3%	0.3%
Hadronic shower	0.3%	0.5%	1.0%	0.4%	0.3%	0.8%
Simulation tune	0.1%	0.1%	0.1%	0.1%	0.1%	0.1%
Detector geometry	0.1%	0.1%	0.2%	0.1%	0.1%	0.5%
Pile-up	0.2%	0.2%	0.1%	0.2%	0.1%	0.1%
OS-SS	1.4%	1.7%	1.9%	1.7%	1.8%	1.8%
Electron	1.3%	0.3%	0.5%	0.6%	0.8%	0.9%
$\Delta \text{SF}^{\text{syst}}$	2.0%	1.9%	2.3%	1.9%	2.0%	2.3%
$\Delta \text{SF}^{\text{stat}}$	1.3%	1.5%	1.9%	1.3%	1.5%	2.0%
$\Delta \text{SF}^{\text{stat+syst}}$	2.4%	2.4%	3.0%	2.3%	2.5%	3.0%
SF	0.992	0.968	0.892	1.002	0.966	0.926

Table 10: $Z \rightarrow \tau_\mu \tau_{\text{had}}$ channel: 1-prong scale factors for all ID working points. The systematic uncertainty from each source is also shown.

$Z \rightarrow \tau_e \tau_{\text{had}}$	1-prong scale factors and uncertainties					
	BDT			LLH		
	Loose	Medium	Tight	Loose	Medium	Tight
Generator	1.5%	1.7%	1.3%	1.5%	1.9%	1.6%
Hadronic shower	0.4%	0.5%	1.4%	0.2%	0.5%	1.0%
Simulation tune	1.1%	1.1%	1.2%	1.1%	1.3%	1.0%
Detector geometry	0.1%	0.1%	0.1%	0.1%	0.1%	0.7%
Pile-up	0.1%	0.1%	0.1%	0.1%	0.1%	0.1%
OS-SS	0.5%	2.0%	3.0%	0.5%	1.3%	1.4%
Electron	0.1%	0.1%	0.3%	0.1%	0.1%	0.6%
$\Delta\text{SF}^{\text{syst}}$	2.1%	2.9%	3.8%	2.0%	2.7%	2.7%
$\Delta\text{SF}^{\text{stat}}$	1.6%	1.8%	2.5%	1.5%	1.8%	2.5%
$\Delta\text{SF}^{\text{stat+syst}}$	2.6%	3.5%	4.5%	2.5%	3.3%	3.7%
SF	1.046	0.983	0.954	1.069	1.004	0.969

Table 11: $Z \rightarrow \tau_e \tau_{\text{had}}$ channel: 1-prong scale factors for all ID working points. The systematic uncertainty from each source is also shown.

$Z \rightarrow \tau_\mu \tau_{\text{had}}$	Multi-prong scale factors and uncertainties					
	BDT			LLH		
	Loose	Medium	Tight	Loose	Medium	Tight
Generator	2.6%	2.1%	2.2%	2.5%	2.7%	1.5%
Hadronic shower	1.3%	1.5%	0.9%	2.8%	1.7%	1.7%
Simulation tune	2.0%	2.2%	2.0%	1.8%	1.7%	0.7%
Detector geometry	1.1%	2.3%	1.1%	0.9%	0.5%	0.1%
Pile-up	0.5%	0.5%	0.6%	0.5%	1.0%	2.0%
OS-SS	2.3%	2.5%	2.9%	2.3%	2.5%	2.9%
Electron	1.7%	0.6%	0.7%	0.6%	0.7%	0.8%
$\Delta\text{SF}^{\text{syst}}$	4.1%	4.3%	3.5%	4.4%	3.9%	3.2%
$\Delta\text{SF}^{\text{stat}}$	1.9%	2.1%	2.8%	1.9%	2.1%	2.8%
$\Delta\text{SF}^{\text{stat+syst}}$	4.6%	4.8%	4.5%	4.7%	4.4%	4.3%
SF	1.149	1.021	0.934	0.998	1.007	0.968

Table 12: $Z \rightarrow \tau_\mu \tau_{\text{had}}$ channel: Multi-prong scale factors for all ID working points. The systematic uncertainty from each source is also shown.

$Z \rightarrow \tau_e \tau_{\text{had}}$	Multi-prong scale factors and uncertainties					
	BDT			LLH		
	Loose	Medium	Tight	Loose	Medium	Tight
Generator	0.5%	0.2%	1.1%	0.3%	0.3%	0.1%
Hadronic shower	1.2%	1.7%	2.1%	0.7%	1.1%	2.3%
Simulation tune	1.6%	1.3%	1.5%	1.4%	1.6%	1.0%
Detector geometry	0.5%	0.5%	0.6%	0.7%	0.4%	0.6%
Pile-up	0.1%	0.1%	0.1%	0.3%	0.1%	0.1%
OS-SS	2.6%	5.1%	7.4%	1.6%	0.7%	5.2%
Electron	0.8%	0.7%	0.6%	0.7%	0.8%	0.7%
$\Delta \text{SF}^{\text{syst}}$	3.3%	5.6%	7.9%	2.4%	2.1%	5.8%
$\Delta \text{SF}^{\text{stat}}$	2.3%	2.6%	3.5%	2.2%	2.6%	3.5%
$\Delta \text{SF}^{\text{stat+syst}}$	4.0%	6.1%	8.7%	3.2%	3.3%	6.8%
SF	1.057	0.998	0.951	1.077	0.994	0.973

Table 13: $Z \rightarrow \tau_e \tau_{\text{had}}$ channel: Multi-prong scale factors for all ID working points. The systematic uncertainty from each source is also shown.

$Z \rightarrow \tau_\mu \tau_{\text{had}}$	Inclusive scale factors \pm syst. unc. \pm stat. unc.		
	Overall	Barrel	End-cap
BDT Loose	$1.001 \pm 2.5\% \pm 1.3\%$	$0.993 \pm 2.7\% \pm 1.8\%$	$1.000 \pm 2.6\% \pm 2.8\%$
BDT Medium	$0.970 \pm 2.4\% \pm 1.5\%$	$0.973 \pm 2.9\% \pm 1.9\%$	$0.947 \pm 2.5\% \pm 2.6\%$
BDT Tight	$0.895 \pm 2.7\% \pm 1.9\%$	$0.930 \pm 3.3\% \pm 2.1\%$	$0.904 \pm 2.4\% \pm 2.6\%$
LLH Loose	$1.001 \pm 2.5\% \pm 1.3\%$	$0.986 \pm 3.1\% \pm 1.8\%$	$0.994 \pm 3.1\% \pm 2.8\%$
LLH Medium	$0.969 \pm 2.6\% \pm 1.5\%$	$0.977 \pm 2.9\% \pm 1.9\%$	$0.929 \pm 2.9\% \pm 2.8\%$
LLH Tight	$0.929 \pm 2.8\% \pm 1.9\%$	$0.912 \pm 3.4\% \pm 2.4\%$	$0.909 \pm 2.9\% \pm 2.9\%$

Table 14: $Z \rightarrow \tau_\mu \tau_{\text{had}}$ channel: scale factors for inclusive $\tau_{\text{had-vis}}$ for all ID working points. The measurement binned in $|\eta(\tau_{\text{had-vis}})|$ is compared to the overall results. The barrel region corresponds to $|\eta(\tau_{\text{had-vis}})| < 1.37$, while the end-cap region corresponds to $|\eta(\tau_{\text{had-vis}})| > 1.52$.

$Z \rightarrow \tau_e \tau_{\text{had}}$	Inclusive scale factors and \pm syst. unc. \pm stat. unc.		
	Overall	Barrel	End-cap
BDT Loose	$1.056 \pm 2.0\% \pm 1.5\%$	$1.040 \pm 2.2\% \pm 1.6\%$	$1.001 \pm 4.4\% \pm 1.9\%$
BDT Medium	$0.996 \pm 3.3\% \pm 1.7\%$	$0.949 \pm 4.5\% \pm 1.9\%$	$0.960 \pm 2.7\% \pm 2.4\%$
BDT Tight	$0.954 \pm 4.8\% \pm 2.3\%$	$0.980 \pm 5.5\% \pm 2.6\%$	$0.911 \pm 5.9\% \pm 4.0\%$
LLH Loose	$1.075 \pm 1.9\% \pm 1.5\%$	$1.054 \pm 2.6\% \pm 1.6\%$	$1.002 \pm 2.7\% \pm 1.9\%$
LLH Medium	$1.002 \pm 2.4\% \pm 1.7\%$	$0.983 \pm 4.1\% \pm 1.9\%$	$0.919 \pm 5.9\% \pm 2.3\%$
LLH Tight	$0.964 \pm 3.3\% \pm 2.3\%$	$0.975 \pm 5.9\% \pm 2.6\%$	$0.886 \pm 4.1\% \pm 3.8\%$

Table 15: $Z \rightarrow \tau_e \tau_{\text{had}}$ channel: scale factors for inclusive $\tau_{\text{had-vis}}$ for all ID working points. The measurement binned in $|\eta(\tau_{\text{had-vis}})|$ is compared to the overall results. The barrel region corresponds to $|\eta(\tau_{\text{had-vis}})| < 1.37$, while the end-cap region corresponds to $|\eta(\tau_{\text{had-vis}})| > 1.52$.

Combination of 1-prong scale factors and uncertainties (%)						
$Z \rightarrow \tau_{\text{lep}} \tau_{\text{had}}$	BDT			LLH		
	Loose	Medium	Tight	Loose	Medium	Tight
SF ($Z \rightarrow \tau_\mu \tau_{\text{had}}$)	0.992	0.968	0.892	1.002	0.966	0.926
uncorr syst.	1.4%	1.7%	1.9%	1.7%	1.8%	1.8%
corr syst.	1.5%	0.7%	2.1%	0.8%	0.9%	1.3%
stat.	1.3%	1.5%	1.9%	1.3%	1.5%	1.9%
syst.+stat.	2.5%	2.4%	3.4%	2.3%	2.5%	2.9%
SF ($Z \rightarrow \tau_e \tau_{\text{had}}$)	1.046	0.983	0.954	1.069	1.004	0.969
uncorr syst.	0.5%	2.0%	3.0%	0.5%	1.3%	1.4%
corr syst.	1.9%	2.1%	2.3%	1.9%	2.4%	2.3%
stat.	1.6%	1.8%	2.5%	1.5%	1.8%	2.5%
syst.+stat.	2.5%	3.5%	4.5%	2.5%	3.3%	3.7%
SF Combination	1.015	0.972	0.908	1.029	0.978	0.940
syst.	1.8%	1.8%	2.7%	1.6%	1.9%	2.1%
stat.	1.0%	1.2%	1.5%	1.0%	1.2%	1.5%
syst.+stat.	2.1%	2.1%	3.1%	1.9%	2.2%	2.6%
ρ (total)	0.457	0.182	0.310	0.251	0.261	0.267

Table 16: $Z \rightarrow \tau_{\text{lep}} \tau_{\text{had}}$ combination: 1-prong scale factors and uncertainties for all ID working points.

Combination of multi-prong scale factors and uncertainties (%)						
$Z \rightarrow \tau_{\text{lep}}\tau_{\text{had}}$	BDT			LLH		
	Loose	Medium	Tight	Loose	Medium	Tight
SF ($Z \rightarrow \tau_{\mu}\tau_{\text{had}}$)	1.149	1.021	0.934	0.998	1.007	0.968
uncorr syst.	2.6%	2.1%	2.2%	2.5%	2.7%	1.5%
corr syst.	3.9%	5.7%	5.3%	4.2%	3.8%	3.7%
stat.	1.9%	2.1%	2.8%	1.9%	2.1%	2.8%
syst.+stat.	5.1%	6.4%	6.4%	5.3%	5.1%	4.9%
SF ($Z \rightarrow \tau_e\tau_{\text{had}}$)	1.057	0.998	0.951	1.077	0.994	0.973
uncorr syst.	2.6%	5.1%	7.4%	1.6%	0.7%	5.2%
corr syst.	2.2%	2.2%	3.0%	1.9%	2.2%	2.6%
stat.	2.3%	2.6%	3.5%	2.2%	2.6%	3.5%
syst.+stat.	4.1%	6.2%	8.7%	3.3%	3.4%	6.8%
SF Combination	1.081	1.008	0.939	1.063	0.996	0.969
syst.	3.5%	4.8%	5.3%	3.0%	2.9%	3.9%
stat.	1.5%	1.7%	2.2%	1.4%	1.7%	2.2%
syst.+stat.	3.8%	5.1%	5.8%	3.3%	3.4%	4.5%
ρ (total)	0.418	0.326	0.282	0.455	0.464	0.294

Table 17: $Z \rightarrow \tau_{\text{lep}}\tau_{\text{had}}$ combination: multi-prong scale factors and uncertainties for all ID working points.